Heat Transfer to Droplets in Developing Boundary Layers at Low Capillary Numbers

A THESIS
SUBMITTED TO THE FACULTY OF THE GRADUATE SCHOOL
OF THE UNIVERSITY OF MINNESOTA
BY

Everett A. Wenzel

IN PARTIAL FULFILLMENT OF THE REQUIREMENTS
FOR THE DEGREE OF
MASTER OF SCIENCE

Professor Francis A. Kulacki

August, 2014

Acknowledgements

I would like to express my gratitude to Professor Frank Kulacki for providing me with the opportunity to pursue graduate education, for his continued support of my research interests, and for the guidance under which I have developed over the past two years. I am similarly grateful to Professor Sean Garrick for the generous use of his computational resources, and for the many hours of discussion that have been fundamental to my development as a computationalist. Professors Kulacki, Garrick, and Joseph Nichols have generously served on my committee, and I appreciate all of their time.

Additional acknowledgement is due to the professors who have either provided me with assistantships, or have hosted me in their laboratories: Professors Van de Ven, Li, Heberlein, Nagasaki, and Ito. I would finally like to thank my family and friends for their encouragement.

This work was supported in part by the University of Minnesota Supercomputing Institute.

Abstract

This thesis describes the heating rate of a small liquid droplet in a developing boundary layer wherein the boundary layer thickness scales with the droplet radius. Surface tension modifies the nature of thermal and hydrodynamic boundary layer development, and consequently the droplet heating rate. A physical and mathematical description precedes a reduction of the complete problem to droplet heat transfer in an analogy to Stokes' first problem, which is numerically solved by means of the Lagrangian volume of fluid methodology.

For Reynolds numbers of order one, the dispersed phase Prandtl number significantly influences the droplet heating rate only in the transient period when the thermal boundary layer first reaches the droplet surface. As the dispersed phase Prandtl number increases, so does the duration of the transient. At later times, when the the droplet becomes fully engulfed by the boundary layer, the heating rate becomes a function of only the constant heat flux boundary condition. This characteristic holds for all Péclet and Weber numbers, but the spatial behavior of the droplet differs for small and large Péclet and Weber numbers.

Simulation results allow for the development of a predictive tool for the boiling entry length of dilute systems in channel flow. The tool relies on an assumption of temperature equivalency between the droplet and the thermal boundary layer evaluated in absence of the dispersed phase, which is supported by the computational results. Solutions for plug and fully developed flow do not differ appreciably, suggesting a precise description of the fluid mechanics is not necessary for an approximation of the boiling entry length. Future experimental work is required to validate the predictive models derived in this thesis.

Contents

List of Figures

Nomenclature

A_s	surface area $[L^3]$	K_d	droplet kinetic energy
a	droplet radius or		$[ML^2/t^2]$
	cross-stream axis $[L]$	$\hat{n}$	normal vector $[L]$
b	streamwise axis $[L]$	P	pressure $[M/Lt^2]$
$Bi = hL/k$	Biot number	$Pr = C_P\mu/k$	Prandtl number
c	color function	q''	heat flux $[M/L^2s^3]$
$Ca = \mu\dot{\gamma}L/\sigma$	Capillary number	R	gas constant $[M/L^2t^2T]$
$C_d = 2F_d/\rho u^2 A_s$	drag coefficient	$Re = \rho uL/\mu$	Reynolds number
C_p	specific heat $[L^2T/t^{-2}]$	r_e	influence radius $[L]$
c_s	speed of sound $[L/t]$	s_T^2	normalized droplet
dx	dimensionless mesh		temperature variance
	spacing	t_p	oscillation period $[t]$
F_d	drag force $[ML/t^2]$	T_v	volume averaged
$\mathbf{F}_{st}$	surface tension $[ML/t^2]$		droplet temperature $[T]$
$Fr = u^2/gL$	Freud number	$\mathbf{u}$	velocity vector $[L/t]$
g	gravitational force	V_j	particle volume $[L^3]$
	$[L^3/Mt^2]$	W	weight function
k	thermal conductivity	$We = \rho u^2 L/\sigma$	Weber number
	$[ML/t^3T]$	$\mathbf{x}$	position vector $[L]$

Greek

α	thermal diffusivity $[L^2/t]$
Γ	interface identifier
$\dot{\gamma}$	shear rate $[L/t^2]$
κ	curvature $[L^{-1}]$
μ	dynamic viscosity $[M/Lt]$
ρ	density $[M/L^3]$
ρ_p	particle number density $[L^{-3}]$
σ	surface tension coefficient $[M/t^2]$
ϕ	generic fluid property
ψ	color function
ψ_i	particle color function
ψ_c	volume averaged color function
Ω	influence region

Subscripts

0	characteristic
∞	farfield
c	continuous
d	dispersed

Superscripts

$*$	dimensionless

Chapter 1

Introduction

1.1 Background

Continued improvement of high power density electronic components requires the development of new thermal management strategies. Many approaches have been proposed, but some of the most promising have been directed toward two-phase convective heat transfer in microchannels. Though it remains an area of considerable promise, transition to film boiling presents a significant disadvantage of single fluid boiling in channels.

After achieving the critical heat flux, any additional thermal energy transfer to the fluid results in the development of an interstitial gas layer that separates the liquid bulk from the heated surface (Thome, 2006). Surface drying promotes rapid elevation of surface temperatures, and potential component malfunction (burnout). The use of a multifluid coolant may reduce or eliminate the risk of burnout.

Implementation of dilute emulsion coolants, rather than single component liquids, has been proposed to extend the temperature range of nucleate boiling

(Roesle and Kulacki, 2010). If the dispersed phase occupies a small percentage of the emulsion by volume, and has a lower boiling point than the continuous phase, the system may benefit from boiling induced mixing and enhanced heat transfer at temperatures well below the boiling point of the continuous phase. Unfortunately, the sparse literature on flow boiling of dilute emulsions has left many questions unaddressed, including that of the boiling entry length, defined as the distance a droplet must travel along a heated surface before boiling.

Prior to boiling, the dispersed phase temperature must increase from the inlet sub-cooled state. Motivation for exploring the heating rate comes from two sources: multifluid heat exchanger design requires knowledge of the boiling entry length, and the interaction of a droplet and a developing boundary layer is an under explored, fundamental problem.

Many researchers have studied droplet heat transfer, but prior studies have not addressed the condition where significant temperature and velocity gradients exist across a small droplet without making assumptions about the droplet thermal diffusivity. In the multifluid microchannel application, droplets do not differ significantly in temperature from the surrounding fluid, but the influence of strong surface tension in the boundary layer may have unforeseen effects on the heating rate. Interactions between the developing boundary layer and the droplet, as a function of deformation and phase dependent properties, cannot be approached with a presently available droplet heat transfer model.

Available heat transfer models prudently apply to many droplet heat transfer problems, but the present literature does not provide a fundamental understanding of small droplet heat transfer in developing boundary layers. The present work seeks to fill this void in the literature, after which the heating rate of a dilute emulsion droplet in a microchannel may be fundamentally described and may serve

as an important design tool. The analysis may additionally be used to determine which dynamics must be included in computation of droplet heat transfer.

1.2 Literature review

An understanding of microchannel fluid dynamics and droplet heat transfer are prerequisites for an informed discussion of this research topic. Reviews of these two fields appear in the following sections.

1.2.1 Microchannel fundamentals

Microchannels have been shown to dissipate energy at a much greater rate than their larger scale counterparts because of reductions in thermal resistance associated with small characteristic lengths and thin boundary layers (Tuckerman and Pease, 1981). The terminology "microchannel" refers generally to small cross-section heat exchangers, typically falling between tens and hundreds of micrometers in characteristic dimension. A precise definition has not been widely accepted, in part because of different behaviors observed in single and two-phase channels (Thome, 2006).

Provided the fluid remains a liquid, the continuum assumption applies and the Navier-Stokes equations govern the system (Kandlikar et al., 2013). Flow characteristics and behaviors observed at the macroscopic scale therefore apply to liquid phase microchannels. After boiling and introduction of the gas phase, instabilities, blow-back, noncontinuum, and slip events become dominant (Kandlikar et al., 2013; Thome, 2006). These behaviors present some of the greatest challenges in two-phase microchannel research, and would be alleviated by the successful implementation of a dilute emulsion coolant.

The Navier-Stokes equations govern continuum liquids, but this does not make microchannel dynamics easily predictable. Fluid motion depends strongly on initial and boundary conditions, and control of boundary conditions becomes challenging at small length scales; small idealizations may result in significant behavioral change. Experimental evidence emphasizes the importance of initial and boundary conditions to predicting microchannel dynamics, but also suggests some useful characteristic behaviors.

Campagnolo et al. (2012) present a measurement of the fully developed microchannel velocity profile. It falls within uncertainty of the Poiseuille velocity profile in a pipe, which asserts a similarity between the fully-developed velocity profiles in macroscopic and microscopic internal flows. Extrapolating the fully-developed similarity to a similarity in the development region requires analytical or experimental support.

The non-linear advection terms present in the Navier-Stokes equations complicate an analytical description of the velocity profile in the entrance region of channels and ducts. Two prominent solution approaches have been integral techniques and linearization of the momentum equation (Sparrow et al., 1964), but these approaches do not provide a closed-form solution, precluding a basic qualitative discussion. Moreover, analytical simplifications and numerical solutions can depart significantly from reality, making empiricism preferable.

Ahmad and Hassan (2010) present a study of the development length in microchannels. Their measurements display a significant flow separation region at the microchannel inlet – precisely the region of interest. It should be understood, therefore, that the velocity profile at the inlet of a microchannel not only depends on Reynolds number and microchannel geometry, but also strongly on the inlet velocity profile.

These few examples show the flow behavior in microchannels to depend greatly on the implementation and the precision of boundary condition control. Knowing this sensitivity, it would be imprudent to assume an inlet velocity profile in a numerical approach, and to suggest the resultant flow evolution to describe the inlet region of a general microchannel. For the purposes of the present study, an approach must be developed that informs the physics in question without over constraining the applicability of the results. More importantly, the general behaviors described here may change with the introduction of droplets.

1.2.2 Droplet heat transfer

Droplet studies have been conducted continuously for centuries, and hundreds (if not thousands) of researchers have studied various droplet behaviors. This review serves only to give the reader a flavor of the field, and to impart a general understanding of the work that have been performed in the past. Special care has been taken to select studies with particular similarity to the present effort, and thus the studies included here relate to the spatial distributions of temperatures in droplets undergoing heat transfer, and to droplet heat transfer modeling. For a more complete review of the field, the unfamiliar reader may refer to one of the many books on the topic, such as Michaelides (2006, 2013).

Spatially resolved heat transfer to droplets

Spatially resolved studies of droplet heat transfer inform model development, provide physical understanding of heat transfer mechanisms, and determine which factors dominantly and negligibly influence droplet behavior. Of concern to this study are trends in transient and spatial temperature variation, the influence of temperature dependent properties, and the dependency of heat transfer on droplet

deformation.

Heat transfer to a droplet depends on droplet geometry, which is determined by the competition between viscous shear and the Laplace pressure in shear flows. With the inclusion of a temperature gradient, the Marangoni effect (defined later in this section) may also become important.

Dai et al. (2002) numerically explore the modification of internal droplet temperature distributions as a function of droplet oscillations. Their study predicts deformation to enhance heat transfer due to increased surface area and the promotion of mixing. Results of cases with droplet Biot numbers of 0.1 and 0.25, coupled with deformations of 0%, 13%, and 35% are presented. Deformation has been defined as the distance between the center of mass and the most distant surface, normalized by the radius of a sphere of equivalent mass. The results show internal temperature distributions to be effectively independent of deformation at $Bi = 0.1$, and a weak function of deformation at $Bi = 0.25$. Departure from the non-deformed temperature distribution increases with increasing oscillation magnitude, but is insignificant in all cases presented.

A similar study performed by Hader and Jog (1998) with forced convection examines heat transfer to a droplet suspended in an immiscible fluid under the influence of an electric field that generates oblate and prolate deformations. The study includes cases where internal droplet heat transfer comprises the primary resistance (internal case, or high Biot number case), as well as the inverse (external case, or low Biot number). For the internal case, numerical results show the external Nusselt number to increase with Péclet number for all deformation types, and for the Nusselt number to become independent of Péclet number at high Péclet numbers. As the Péclet number increases, prolate deformations display greater Nusselt numbers than oblate deformations (Figure 1.1(a), where the cross-stream

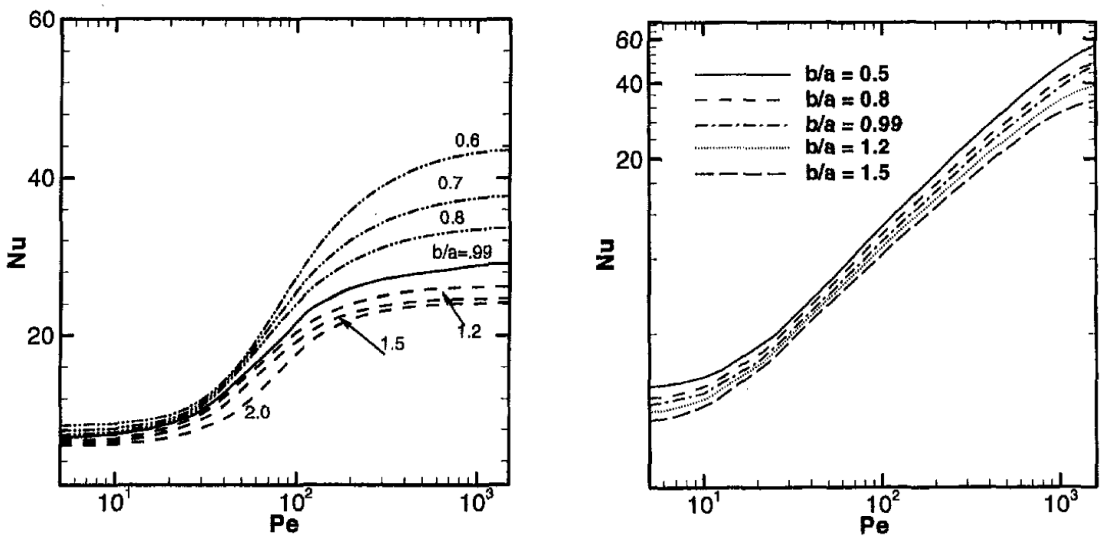

(a) High Biot number droplet heat transfer

(b) Low Biot number droplet heat transfer

Figure 1.1. Convective heat transfer to deformed droplets at high and low Biot numbers (Hader and Jog, 1998).

and streamwise axes are given by a and b, respectively). For the external case, shown in Figure 1.1(b), droplet deformation negligibly modifies heat transfer. At low relative velocity between phases, droplet deformation negligibly affects the Nusselt number for both deformation types, whereas the Nusselt number has a strong dependency on droplet geometry at high relative velocities for the high Biot number case.

Both Dai et al. (2002) and Hader and Jog (1998) cite the promotion of internal circulation as one of the heat transfer mechanisms of droplet deformation, and experimental results presented by Wong and Lin (1992) verify the presence of counter-rotating vortices inside droplets suspended in convective flows. The parameter space includes Reynolds numbers of approximately 17, 60, and 100. The qualitative nature of the circulation, according to the data, appears independent

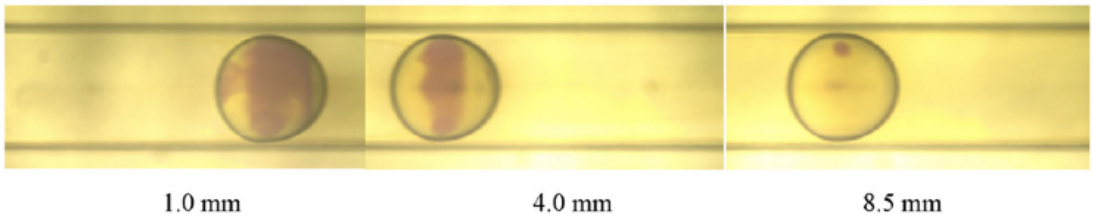

Figure 1.2. Hill vortices in reacting droplets (Xu et al., 2008).

of external Reynolds number, but has strong dependency on droplet viscosity; liquid droplets with lower viscosities experience greater heat transfer due to internal circulation than higher viscosity liquids. This study also compares the experimental results to three commonly used analytical models, namely the conduction limit, the vortex, and the effective conductivity models, which appear in the next section of this chapter.

Antar et al. (2000) present a finite difference study that explores convective heat transfer to droplets. Their results suggest increasing either the external Reynolds number or the exterior to interior viscosity ratio increases energy transfer to the droplet. Both of these parameters essentially facilitate internal circulation, and the mixing of energy and species.

Assuming a decoupling of the momentum and energy equations, the heat and mass transfer analogy applies. Xu et al. (2008) experimentally examine mass transfer across the interface of an aqueous NaOH droplet suspended in a channel flow of n-butanol. Figure 1.2 displays the general mixing behavior, where the light and dark colors indicate product and reactant, respectively. The lengths displayed below the images indicate travel distance along the channel. As the travel distance increases, the internal swirling motions facilitate the reaction. Departure from spherical geometry appears minimal, as does the relative velocity between phases. This suggests a dominance of surface tension over viscous forces, but the authors

do not provide a discussion of the relevant dimensionless groups. Increases in flow velocity result in increased mass transfer rates, but the authors do not propose a mechanism. Boundary layers present in the internal flow promote this circulation, and the general interaction of velocity gradients with droplets has been explored by other researchers.

Dandy and Dwyer (1990) numerically treat the lift, drag and heat transfer experienced by a particle suspended in shear flows of uniform temperature. Their results suggest the heat transfer rate to be independent of the shear rate for constant Reyonlds numbers. The free-steam velocity associated with the particle centerline allows for determination of an average Nusselt number. More commonly researchers have explored the case of droplets traveling through a continuous phase with a well-defined velocity difference, rather than a droplet in shear.

To address concerns in the nuclear power industry, Huang and Ayyaswamy (1987) numerically analyze heat and mass transfer to a single water droplet falling under the influence of gravity with a horizontal velocity component. The researchers examine the effects of droplet size, initial velocity, and initial trajectory on the fall height required for thermal equilibrium. As expected, larger droplets require greater fall heights to reach stable dimensionless bulk temperatures. Fall heights also decrease with increasing horizontal velocity. Greater initial velocities increase heat and mass transfer to the droplets, in agreement with the findings of Dandy and Dwyer (1990). These studies assume uniform surface tension, but this assumption does not always apply.

Temperature dependent surface tension phenomena is often referred to as the thermocapillary effect, or the Marangoni effect. This behavior is important in some applications because a surface tension gradient induces fluid motion in droplets. Niazmand et al. (1994) numerically explore thermocapilary effects on

droplet evaporation and heating. They suggest thermocapilary effects may be assumed small when,

$$\Delta T << a\rho_\infty {U_\infty}^2 C_D \left(\frac{\partial \sigma}{\partial T}\right)^{-1}, \tag{1.1}$$

or,

$$\Delta T << \mu_\infty Re^2 C_D \left(4a\rho_\infty \frac{\partial \sigma}{\partial T}\right)^{-1}. \tag{1.2}$$

Savino and Fico (2004) couple numerical and experimental techniques to examine the effects of Marangoni convection on the internal temperature distribution of a droplet suspended below a heated/cooled plate. Their findings show that Marangoni convection increases with decreasing fluid viscosity. The results also display a far more uniform temperature field in the cases with strong Marangoni convection compared to cases with weak Marangoni convection.

Frackowiak et al. (2010) use direct numerical simulation (DNS) to examine a train of evaporating fuel droplets and notice a significant influence of the Marangoni effect. At times, the Marangoni stress exceeds the viscous stress in magnitude, which results in three counter-rotating vortices, departing from the two vortex circulation mode displayed in Figure 1.2. Similarly, Raghuram et al. (2012) present a study on the relative strength of Marangoni and forced convection in an evaporating, multicomponent droplet suspended in cross flow. Marangoni convection dominates at low free stream velocities (small particle Reynolds numbers) and forced convection dominates at high free stream velocities (high particle Reynolds numbers). The relative influence of these two phenomena manifest in the direction of internal circulation. Marangoni dominance associates with a change in the sign of velocity at the droplet interface, whereas viscous dominance does not.

Droplet heat transfer models

Droplet heat transfer models allow for analytical approximations to complicated problems and often reduce the numerical load of computational approaches. Frequently used models appear in this section with reference to their assumptions, accuracy, and ease of implementation.

Every model makes assumptions of varying physical and mathematical implication, resulting in varying accuracy and ease of use. Droplet heating models may be partitioned into six general categories (Sazhin et al., 2006): isothermal droplets (with application to boiling problems); spatially isothermal droplets (an assumption of infinite thermal diffusivity); solid droplets with spatially and temporally variable temperature (the conduction limit); conduction limit models that implement an effective thermal conductivity in an attempt to account for the thermal effects of convection; droplets with prescribed internal convection; and fully-resolved Navier-Stokes solutions.

Application of the isothermal droplet model requires an understanding of the lumped capacitance assumption. Moreover, a refined understanding of the lumped capacitance assumption enriches one's perspective on droplet heat transfer in general, and lowers the risk of imprudent model selection. For this reason, the lumped capacitance model (LCM) deserves treatment with an emphasis on dimensionality to place the intricacies of the method on the forefront.

Transient temperature variation within a system depends on the rate of energy addition at the system boundary and the rate of energy transfer away from the boundary. Spatial temperature variation depends on the relative magnitude of these two rates through the Biot number,

$$Bi = \frac{hL_0}{k}, \tag{1.3}$$

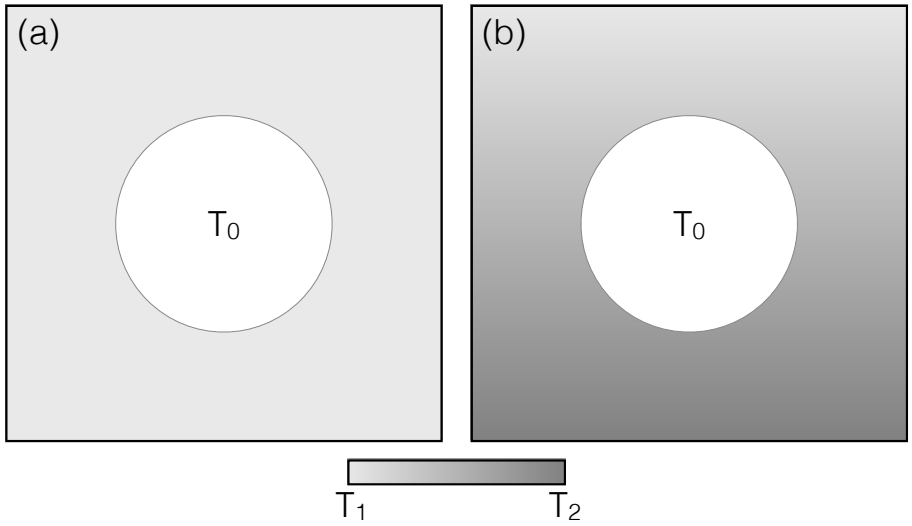

Figure 1.3. Droplets exposed to (a) uniform and (b) variable temperature fields.

where L_0 is a characteristic length, h is the boundary heat transfer coefficient, and k is the thermal conductivity. Large Biot numbers denote spatially variable temperature, while small Biot numbers denote spatially uniform temperature. In the case of a small Biot number, the LCM provides considerable simplification.

The LCM enforces spatial uniformity of temperature within the domain it applies. Its application has been accepted for cases where $Bi << 1$, and reduces the thermal energy equation to a first-order, linear differential equation,

$$\rho C_p \frac{\partial T}{\partial t} = q'' A_s, \tag{1.4}$$

which relates the change of thermal energy contained in a system (the l.h.s. of Eqn. (1.4)) to the transfer of energy across the system boundary (the r.h.s. of Eqn. (1.4)). Application of the LCM is a robust simplification in certain situations, but comes with the cost of reduced dimensionality.

Consider the problem domain in Figure 1.3(a), which depicts a droplet of temperature T_0 suspended in a quiescent fluid of temperature T_1. The problem may be described by a one-dimensional thermal resistance circuit because of spherical symmetry and a uniform farfield temperature. If $h^{-1} >> a/k$ (where a is the droplet radius), the conduction resistance, a/k, may be neglected. With this assumption, the temperature inside the droplet adheres to Newton's Law of Cooling, given by

$$T(t) = T_1 - (T_1 - T_0)\exp\left(-\frac{hA_s}{\rho C_p}t\right). \tag{1.5}$$

Errors resulting from this assumption become vanishingly small despite the reduction in dimensionality when the Biot condition is well satisfied, but the dimensional reduction does not always apply.

Suppose the temperature field depends on a spatial dimension, as in Figure 1.3(b). In this case, a low Biot number droplet maintains a uniform temperature, but enforcing temperature continuity modifies the external temperature field. With a variety of options, selection of a characteristic temperature difference becomes difficult for nontrivial geometries, and introduction of convection further complicates the mathematics.

Michaelides and Feng (1994) present an analytical model used to quantify heat transfer from a sphere in non-uniform velocity and temperature fields. Their model includes, in part, an assumption of high thermal conductivity in the sphere relative to that of the surrounding fluid. This model does not apply to the type of problem addressed by this thesis, considering the high continuous phase thermal diffusivity in heat transfer liquids (almost certainly comparable or greater than the dispersed phase). Although the Michaelides and Feng (1994) solution accounts for a spatially variable temperature field, most models have been designed for use in a uniform farfield temperature.

The conduction limit, the effective conductivity, the vortex, and the lumped capacitance models traditionally require a spatially uniform external temperature field. Applications of interest have historically satisfied this requirement, and the assumption has been implemented because it allows for significant simplification. With the implications of the LCM and uniform farfield temperatures in mind, an elaboration on droplet heat transfer models may begin with the effective conductivity model.

Kronig and Brink (1951) first introduce the concept of effective diffusivity in droplets. Their study presents rates of mass extraction from droplets suspended in an immiscible liquid in stationary and moving conditions. When considering the average rate of mass extraction, the results for the diffusion and diffusion plus advection cases differ by a factor of 2.5, which allows for the construction of an effective diffusivity. In prediction of mass extraction rates, the effective diffusivity allows for the solution of the diffusion problem, rather than the combined convection-diffusion problem.

Abramzon and Sirignano (1988) extend the effective thermal conductivity concept by developing an empirical correlation for the experimental data of Johns and Beckmann (1966), given by,

$$\frac{k_{eff}}{k} = 1.86 + 0.86\tanh\left[2.245\log_{10}\left(Pe_L/30\right)\right], \tag{1.6}$$

where Pe_L is the Peclet number evaluated inside the droplet, k is the droplet thermal conductivity, and k_{eff} is the effective thermal conductivity accounting for internal circulation. Quality results require an accurate evaluation of Pe_L.

Sazhin et al. (2005) begin their discussion by contesting the application of infinite thermal conductivity models (equivalent to the LCM) to numerical codes has occurred simply because of computational efficiency; physical reasoning does not

support the assumption in many instances. They follow this contention with the development of an analytical model of droplet evaporation and heat transfer that addresses internal heat conduction, external convection, radiation, and evaporation. Their model, similar to many others, requires spherically symmetric heating of the droplet. They find their model (after assuming a constant surface heat transfer coefficient) to better balance accuracy and computational efficiency than the fully discretized heat conduction equation, the infinite thermal conductivity assumption, and an assumption of a parabolic temperature distribution.

Models that incorporate motion interior to the droplet add a layer of complexity to the analysis. Moore (1962) and Harper and Moore (1968) present among the first models for internal droplet motion suspended in a fluid of similar properties. Their analytical work allows for the calculation of internal circulation, which differs slightly from that of a Hill vortex because of boundary layers generated by unmatched shear stress at the interface. Prakash and Sirignano (1977) extend the work of Harper and Moore (1968) to a liquid droplet in a gaseous environment. More importantly, they discuss the heat transfer problem, and argue that their results discount the use of a uniform temperature assumption.

Solution of the full Navier-Stokes equations provides the most complete and accurate description of droplet behavior. As suggested by Sazhin et al. (2006), the cost of this approach prohibits its use on a large scale. However, for the generation of fundamental understanding, experimentation serves as perhaps the only alternative.

1.3 Scope of the present study

The problem at hand is the heating rate of an emulsion droplet in the near-wall region of a laminar boundary layer, generally motivated by multifluid microchannel applications. A direct solution of the entire physical problem would generate numerous original contributions, but the variability of important parameters between different microchannels can be extreme. Instead, this thesis seeks to develop an understanding of the near-wall droplet heat transfer regime in general, to inform the boiling entry length, and to lend perspective on near-wall dispersed phase modeling.

Characteristic features of droplet heat transfer in boundary layers include differences in Prandtl number between the continuous and dispersed phases, droplet deformation and resultant modifications to the boundary layer profile, thermocapillary effects, and flow features associated with the Péclet number. Thermocapillary effects are neglected here, but serve as a source of future work. Exhaustive coverage of the remaining parameters cannot be performed in one effort, but the general behaviors associated with each can be explored. This thesis describes how the heating rate of a droplet depends on deformation and the continuous to dispersed phase Prandtl number ratio at Péclet numbers appropriate for the near-wall region in a microchannel. The results are used to inform the boiling entry length and dispersed phase modeling in boundary layers.

Chapter 2

Analytical Formulation

Droplets adhere to the Navier-Stokes equations: conservation of mass, momentum, and energy. The primary challenge in applying the Navier-Stokes equations to droplets, and to multiphase systems in general, relates to the number and complexity of the boundary conditions. The mathematical nature in which these boundary conditions appear depends on the perspective of the governing equations. As a precursor to the development of a numerical approach, this chapter presents an Eulerian formulation of the Navier-Stokes equations appropriate for multiphase systems.

2.1 An Eulerian perspective on multiphase systems

Property variations in multiphase systems impede the development of Eulerian governing equations. Consider the canonical Eulerian Navier-Stokes equations for

incompressible fluids,

$$\nabla \cdot \mathbf{u} = 0, \tag{2.1}$$

$$\frac{\partial(\rho \mathbf{u})}{\partial t} + \mathbf{u} \cdot \nabla(\rho \mathbf{u}) = -\nabla p + \nabla \cdot (\mu \nabla \mathbf{u}) + \mathbf{F}, \tag{2.2}$$

$$\frac{\partial(\rho C_p T)}{\partial t} + \nabla \cdot (\rho C_p T \mathbf{u}) = \nabla \cdot (k \nabla T). \tag{2.3}$$

Non-dimensionalization of these equations involves the introduction of characteristic scales and the extraction of constants from derivative operators. Fluid properties must remain within derivative operators in multiphase systems because of their discontinuous variation at interfaces. Interfacial tension accompanies property discontinuities, introducing further spatio-temporal variability. These challenges require a general formulation that allows for spatial property variation and at least two distinct phases.

Consider a domain that contains a continuous phase, c, and a dispersed phase, d, that interact across an interface, Γ. The phase identifying function, ψ, provides a spatially dependent, mathematical definition of phase,

$$\psi(\mathbf{x}) = \begin{cases} 0 & \text{if in } c; \\ 1 & \text{if in } d. \end{cases} \tag{2.4}$$

For an analytical formulation, the Heaviside nature of ψ poses no issues, but the discontinuity must be smoothed for a numerical approach. Considering this to be an analytical formulation, the phase identifying function may be used to mathematically inform the spatial variation of properties and interfacial momentum sources.

Fluid properties specific to c and d may be defined as a function of ψ,

$$\Phi = \Phi_c(1 - \psi) + \Phi_d\psi, \tag{2.5}$$

where Φ represents a fluid property, and subscripts c and d denote the phase-specific property. Wherever the phase identifying function changes in magnitude (on a line segment in two dimensions, or on a surface in three dimensions), an interfacial tension force appears.

Interfacial tension acts normal to Γ due to phase discontinuity and is quantified by,

$$\mathbf{F}_{st}\Big|_{\Gamma} = -\kappa\sigma\hat{n}, \tag{2.6}$$

where κ is the radius of curvature of Γ, $\hat{n}$ is the outward-directed normal, and σ is the coefficient of interfacial tension. This force acts only at the interfacial line or surface and equals zero elsewhere. Precise representation of σ requires experimentation, but Antanow's Law, given in Eqn. (2.7), provides an analytical alternative (Berg, 2010). Here, $\sigma_{c,d}$ is the interfacial tension coefficient of phases c and d, and the terms on the r.h.s. are the mutually saturated surface tensions of phases c and d.

$$\sigma_{c,d} = \left|\sigma_{c(d)} - \sigma_{d(c)}\right| \tag{2.7}$$

Using these new definitions, appropriate scaling factors may be selected,

$$t^* = \frac{tu_0}{L_0}, \qquad \mathbf{x}^* = \frac{\mathbf{x}}{L_0}, \qquad T^* = \frac{T}{T_0}, \qquad P^* = \frac{P}{\rho_0 {u_0}^2}, \tag{2.8}$$

where subscript naught refers to a characteristic variable chosen to scale a specific problem. When the properties of the continuous and dispersed phases differ, they cannot be completely absorbed by the traditional dimensionless numbers (such as the Reynolds and Prandtl numbers). Instead, dimensionless properties must

assume the color function as an argument,

$$\Phi^* = \psi + \frac{\Phi_c}{\Phi_d}(1-\psi), \tag{2.9}$$

where the dimensionless property equals one in the dispersed phase, $\psi = 1$, and the ratio of the dimensional fluid properties in the continuous phase, $\psi = 0$. Equation (2.9) implies the traditional dimensionless numbers must share control of the system behavior with the dimensionless property ratios, which causes the behavioral changes associated with phase interfaces in multiphase systems. This topic appears once more in the next section for emphasis and clarity.

The Navier-Stokes equations may be reformulated in dimensionless variables appropriate for an incompressible, multiphase system (omitting the asterisks),

$$\frac{\partial \rho}{\partial t} = -\frac{\partial(\rho u_i)}{\partial x_i}, \tag{2.10}$$

$$\frac{\partial(\rho u_i)}{\partial t} + \frac{\partial(\rho u_i u_j)}{\partial x_j} + \frac{\partial P}{\partial x_i} = \frac{1}{Re}\frac{\partial}{\partial x_i}\left(\mu\frac{\partial u_i}{\partial x_j}\right) + \frac{\rho}{Fr} - \frac{\sigma\kappa}{We}, \tag{2.11}$$

$$\frac{\partial(\rho C_p T)}{\partial t} + \frac{\partial(\rho C_p T u_i)}{\partial x_i} = \frac{1}{RePr}\frac{\partial}{\partial x_i}\left(k\frac{\partial T}{\partial x_j}\right), \tag{2.12}$$

where Re is the Reynolds number, Pr is the Prandtl number, Fr is the Froude number (the ratio of kinetic energy to gravitational potential energy), and We is the Weber number (the ratio of kinetic energy to surface tension). The fluid properties present in Eqns. (2.10-2.12) are defined as in Eqn. (2.9). The dimensionless

numbers have been constructed with respect to the dispersed phase such that,

$$Re = \frac{\rho_d u_0 L_0}{\mu_d}, \tag{2.13}$$

$$Fr = \frac{u_0^2}{g L_0}, \tag{2.14}$$

$$We = \frac{\rho_d u_0^2 L_0}{\sigma}, \tag{2.15}$$

$$Pr = \frac{C_d \mu_d}{k_d}. \tag{2.16}$$

The importance of these dimensionless numbers and others that do not appear in the governing equations to appropriately locate a problem in the parameter space merits particular treatment.

2.2 Dimensionless variables, scaling, and problem formulation

Multiphase systems involve more dimensionless parameters than single phase systems to account for property variations and surface tension. The Reynolds and Prandtl numbers appear, as they do in single phase problems, but the Freud number and the Weber number appear as well. Introducing gravitational forces would over extend the present work, and are neglected by setting the Freud number equal to infinity. A more significant parameter, although it does not appear in the governing equations, is the Capillary number.

Defined as the ratio of viscous shear stress to the Laplace pressure, the Capillary number describes the deformation and breakup of a droplet in shear flow (Li

et al., 2000). With respect to flow variables,

$$Ca = \frac{\mu_c \dot{\gamma} a}{\sigma}, \tag{2.17}$$

where μ_c is the kinematic viscosity of the continuous phase, $\dot{\gamma}$ is the flow shear rate, a is the droplet radius, and σ is, again, the interfacial tension coefficient.

Surface tension dominates and allows little deformation at low Capillary numbers. As the Capillary number increases, steady deformation occurs, and eventually the droplet experiences unsteady breakup at a critical Capillary number (Li et al., 2000; Stone et al., 1986). Considering this behavior, it is expected that the interaction of a droplet and a boundary layer depends on the Capillary number magnitude. If this is the case, the Capillary number should be somehow related to the governing equations, despite their formulation in terms of a characteristic velocity rather than a characteristic shear rate.

The dominating flow characteristic in shear flows is not a mean velocity, but rather a mean rate of shear. In these cases, the pertinent Reynolds number is the shear Reynolds number,

$$Re_{\dot{\gamma}} = \frac{\rho_c \dot{\gamma} a^2}{\mu_c}, \tag{2.18}$$

where the appropriate length scale is the droplet radius, a. The Weber number may be similarly redefined,

$$We = \frac{\rho_d \dot{\gamma}^2 a^3}{\sigma}. \tag{2.19}$$

The relation between the shear Reynolds number, the Weber number, and the Capillary number is therefore (assuming a continuous to dispersed phase density ratio of one)

$$Ca = \frac{We}{Re_{\dot{\gamma}}}. \tag{2.20}$$

For a droplet to remain relatively undeformed by a developing boundary layer,

$$We << Re_{\dot{\gamma}}. \tag{2.21}$$

Significant deformation or breakup occurs if the Weber number exceeds the shear Reynolds number. Rigorously, the critical Capillary number depends on multiple factors including the Reynolds number and the continuous to dispersed phase viscosity ratio (meaning it cannot be identified simply by the magnitude of We/Re_{γ}), but these dependencies are neglected here.

One can imagine the local shear Reyonolds number to be large near a boundary and small far from the boundary. Similarly, the Weber number of a large droplet exceeds that of a small droplet. Characteristic magnitudes for both of these parameters must be chosen to identify where the problem in question falls within the parameter space, which involves selecting characteristic properties, length, and velocity scales.

Following the experimental precedence of Roesle and Kulacki (2012), a 10 μm diameter droplet of FC-72 is a candidate dispersed phase. The most rapidly heating droplets would be those nearest the surface, and therefore the droplet center should be considered a few droplet radii from the heated boundary. Flow velocities may be approximately 10 cm/s in a microchannel or mini channel, which serves as a reasonable characteristic velocity. The Weber and Reynolds numbers for these scales are on the order

$$We = O(0.01)$$

and

$$Re_{\dot{\gamma}} = O(1.0).$$

As made clear by the preceding analysis, a vast parameter space of We and $Re_{\dot{\gamma}}$ exists, not only across different microchannels and in different flow regimes, but also within a single microchannel, depending on droplet size, constitution, and location relative to the wall. Thus, the above Weber and Reynolds numbers only serve as a references. Although selecting different values for these parameters would influence deformation, the change in deformation alone would only mildly modify heating rates (Dai et al., 2002), which depend more strongly on the Péclet and Prandtl numbers.

In an effort to be rigorous, it must be made clear that the Péclet number, as the product of Prandtl and Reynolds numbers, absorbs all variations in Prandtl number. When formulating multiphase problems in a dimensionless sense, difficulties arise as to which fluid properties and flow parameters serve as characteristic. In the uncharacteristic phase, the normalized properties present in Eqns. (2.10-2.12) become active (non-unity). These active properties in the multiphase formulation introduce spatial variations that may dominate the perceived scaling. One example is a dispersed phase with a high Prandtl number in a continuous phase of low Prandtl number. In a non-dimensionalization with respect to the dispersed phase, the global Péclet number may be small, but the effective Péclet number in the continuous phase remains large, resulting in dramatically different behavior within the different phases. It should be understood that referring to the Péclet and Prandtl numbers independently makes reference to variation in the uncharacteristic Prandtl or Péclet number.

As shown by the results of Hader and Jog (1998) (Figure 1.1), the Nusselt number depends greatly on the Péclet number and the Biot number. Many of the droplet heating models described in Chapter 1 require a low Biot number assumption because it considerably simplifies the calculation. To explore the effects of the

Biot and Péclet numbers in the flow regime at hand, the continuous phase Péclet number assumes two values by setting the continuous phase Prandtl number, Pr_c, equal to unity for all simulations, and modifying the Reynolds number from 1 to 5. For each continuous phase Péclet number, the dispersed phase Prandtl number, Pr_d, assumes magnitudes of 0.2, 1.0 and 5.0. This provides cases where the continuous phase thermal diffusivity is high, equivalent, and low compared to the dispersed phase thermal diffusivity, which are the high and low Biot number conditions. These permutations have been selected to provide insight on how the present heat transfer regime may differ from that of traditional droplet heat transfer (uniform far-field temperature and free-stream velocity). The domain most appropriate to feasibly accomplish this task remains an important question.

2.3 Flow domain – initial and boundary conditions

The environment of interest is a developing boundary layer and the nature of its interaction with a droplet. As suggested in Chapter 1, an attempt to model a characteristic microchannel boundary layer would fall short for a variety of reasons: boundary layer development differs in round, square, and rectangular microchannels (Sparrow et al., 1964); the velocity gradients near the channel inlet depend strongly on the inlet flow profile (Kiya et al., 1972); and flow separation may greatly modify behavior in the inlet region (Ahmad and Hassan, 2010). Knowing the importance of these inconsistencies, the selected boundary layer must display generality to inform behavior in the greatest number of applications.

Stokes' first problem describes the development of a one-dimensional boundary layer. This study benefits from a one-dimensional configuration because it most

simply isolates the development of a boundary layer into a droplet, and it does not include characteristics that are variable between different microchannel configurations, such as separation or an accelerating free-stream. Classical boundary layer theory suggests that gradients in the velocity-normal direction exceed those in the streamwise direction by orders of magnitude, and neglecting variations in the streamwise direction is therefore consistent with the problem physics. This feature of Stokes' first problem conveniently lends itself to the use of periodic boundary conditions in the streamwise direction, which dramatically reduces computational cost. Another difference between Stokes' first problem and an internal boundary layer are the boundary conditions in the velocity-normal directions.

The maximum velocity in an external flow is constant (for $dP/dx = 0$), whereas the maximum velocity in an internal flow increases until the fully-developed condition. This difference does not degrade the quality of results generated by an external flow because the rate of change of maximum velocity differs from geometry to geometry, and therefore solving the parallel plate problem would say no more about the round tube case than the Stokesian boundary layer. Having established Stokes' first problem as a reasonable environment for this analysis, attention may be directed to constructing numerically feasible boundary conditions.

Figure 2.1 shows the problem domain, the initial droplet location and size, and the initial temperature and velocity fields,

$$T(y) = 1 - \tanh[1.5(y + 4.5)], \tag{2.22}$$

and

$$u(y) = \tanh[1.5(y + 4.5)]. \tag{2.23}$$

All parameters appearing in Figure 2.1 are nondimensional.

Some obvious difference between the domain presented in Figure 2.1 and the

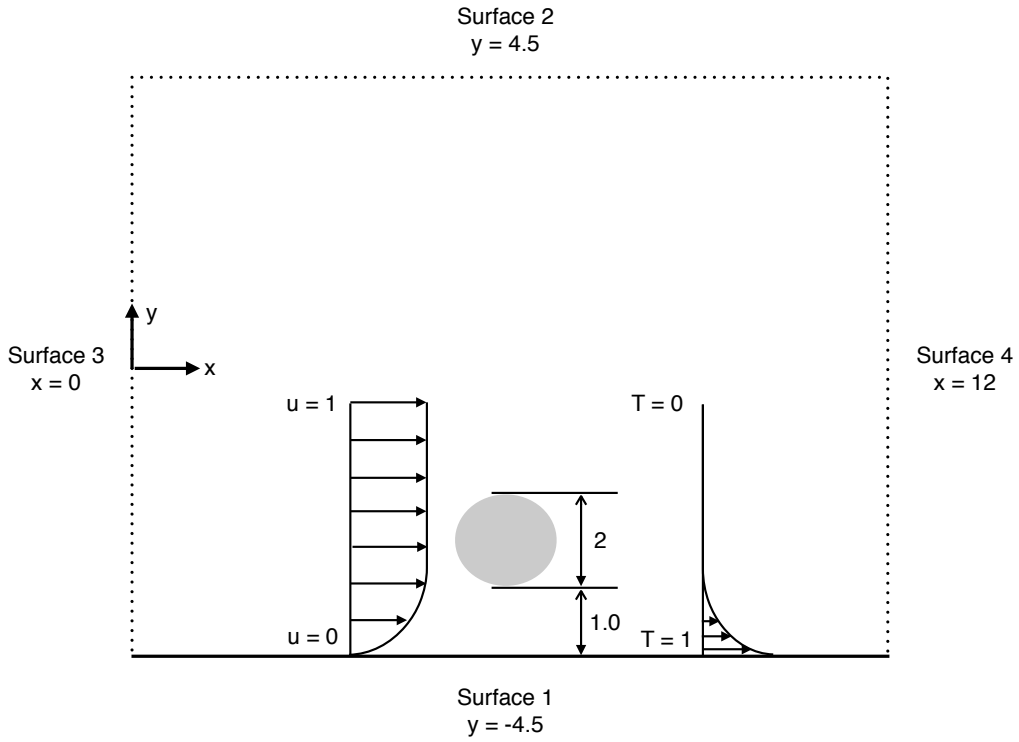

Figure 2.1. Problem domain.

classical Stokes' first problem include: diffusion of velocity from the free stream to the surface, rather than from the surface to the free stream; a numerically differentiable, rather than a discontinuous initial condition; and a finite, rather than an infinite domain. The first difference has been implemented in reference to the cooling application (fluid flowing over a surface, rather than a surface moving under a fluid), while the second and third are numerical necessities. The profiles have been chosen to smoothly transition the velocity from zero to one, and the temperature from one to zero in the region between Surface 1 and the droplet. At

Surface 1,

$$\left.\frac{\partial T}{\partial y}\right|_{y=-4.5} = -1.5, \tag{2.24}$$

while the velocities satisfy the no-slip and no-penetration conditions. At Surface 2, the derivatives of all flow properties in the y direction equal zero, while periodic boundary conditions govern Surfaces 3 and 4. The domain height and width have been selected to minimize the influence of the boundary conditions on the droplet dynamics.

Surface tension generates the Laplace pressure when a curved surface separates the continuous and dispersed phases. For a static droplet, the pressure difference between the exterior and interior fluid may be calculated by considering the droplet radius,

$$\Delta P = \frac{\sigma}{a}, \tag{2.25}$$

in physical units, and in a dimensionless sense,

$$\Delta P^* = \frac{1}{We}, \tag{2.26}$$

where the characteristic length is taken to be the droplet radius. Conversely, density variations across an interface in incompressible systems do not depend on the interface geometry. The precise initialization of density and pressure used to for the present calculations appear after a presentation of the numerical technique.

Chapter 3

Numerical formulation

This chapter outlines the chosen methodology regarding interface tracking, the numerical representation of fluid properties and surface tension, and the governing equation formulation.

3.1 Interface tracking

Interface identification and propagation provides a significant challenge for multiphase numerical simulation. To date, two of the most popular interface identification techniques are the volume of fluid (VOF) (Hirt and Nichols, 1981) and the level set (LS) (Osher and Sethian, 1988). Both the VOF and LS belong to the front capturing classification, a subset in the broad spectrum of phase identification approaches. Multiple researchers have conducted substantial reviews of the numerous techniques, but a review does not appear here; the curious reader may refer to Morris (2000), Abgrall and Karni (2000), or Nourgaliev et al. (2004). Instead, this section outlines some of the shortcomings associated with the popular LS and VOF methodologies, and presents a method which does not suffer from

the same shortcomings.

The VOF method uses a color function, c, which equals 1 in one phase and 0 in the other phase, to generate an Eulerian phase identity. The color function advances in time according to the advection equation,

$$\frac{\partial c}{\partial t} + \mathbf{u} \cdot \nabla c = 0. \tag{3.1}$$

The left-hand-side of Eqn. 3.1 is equivalent to the material derivative and equals zero. This makes the color function a conserved quantity, and allows the VOF method to conserve mass with respect to both phases – an important physical consistency. However, advancing Eqn. (3.1) produces numerical diffusion and the spatial smearing of the interface, which physically represents mutual diffusion of the phases. Numerical diffusion non-physically changes the interface over time and represents a significant disadvantage of the VOF method. The LS method does not suffer from interface smearing.

Instead of advecting the color function (by means of Eqn. (3.1)), the LS method uses a function to indicate the distance from any point to the interface, with the distance positive in one phase and negative in the other. A change in sign of the distance function identifies a phase transition. With the LS approach, the interface remains sharp, but conservation of the signed-distance function does not enforce mass conservation. It should be understood that both the LS and VOF methods introduce significant non-physical behavior into the solution, which amplifies greatly when applied on unstructured meshes.

The Lagrangian volume of fluid method (Liu, 2014; Liu et al., 2014) uses Lagrangian phase-identifying particles to track fluid interfaces. By using a Lagrangian perspective, LVOF eliminates the diffusion and conservation issues associated with traditional VOF and LS, respectively. It may also be accurately

implemented on unstructured meshes. The calculation approach originates from smoothed particle hydrodynamics (SPH), and a basic understanding of SPH is a necessary prerequisite to understanding LVOF.

3.1.1 Smoothed particle hydrodynamics

Smoothed particle hydrodynamics assumes that a function, f, may be approximated by a convolution of the function with a kernel,

$$\langle f(\mathbf{x})\rangle = \int_{\Omega} f(\mathbf{x}')\, W(\mathbf{x}-\mathbf{x}'; r_e)\, d\mathbf{x}', \tag{3.2}$$

where W is the kernel (or weight) function, which is non-zero over an influence radius, r_e (Randles and Libersky, 1996). Following the convolution operation, $\langle f(\mathbf{x})\rangle$ is considered the kernel representation of the function, f. Fidelity of the kernel representation to the function itself strongly depends on the nature of the kernel.

The kernel serves as an approximation of the Dirac delta function and may assume any definition satisfying the series of conditions elaborated by Liu and Liu (2010). These conditions effectively guarantee that the kernel approaches the Dirac delta function as the influence radius approaches zero, resulting in a vanishing error. Using the kernel representation of a function is favorable because it allows for the kernel representation of derivatives.

For an appropriately defined kernel, application of the chain rule shows that the gradient of f equals the product of f and the gradient of the kernel (Randles and Libersky, 1996),

$$\langle \nabla f(\mathbf{x})\rangle = \int_{\Omega} f(\mathbf{x}')\, \nabla W(\mathbf{x}-\mathbf{x}'; r_e)\, d\mathbf{x}'. \tag{3.3}$$

Special note should be taken that the kernel representation of the derivative depends only on the derivative of the kernel, and not on the derivative of the function. This property is beneficial because ∇W often has an analytical expression, whereas the computation of ∇f requires numerical methods. Moreover, the derivative of the kernel is not complicated by a discrete representation.

Discretely recasting the kernel representations of f and ∇f returns,

$$\langle f(\mathbf{x})\rangle = \sum_{j=1}^{N} V_j f(\mathbf{x}_j) W(\mathbf{x}-\mathbf{x}_j; r_e), \tag{3.4}$$

and

$$\langle \nabla f(\mathbf{x})\rangle = \sum_{j=1}^{N} V_j f(\mathbf{x}_j) \nabla W(\mathbf{x}-\mathbf{x}_j; r_e), \tag{3.5}$$

respectively, where V_j is the volume associated with the discrete element or particle, j. Discrete formulations lend themselves to numerical treatment, but also have shortcomings.

Particle inconsistency in the kernel approximations arise in special cases, particularly for boundary particles (Liu and Liu, 2010). Generally, inconsistency in the kernel itself may be used to mitigate inconsistency in the kernel representation (Randles and Libersky, 1996),

$$\langle f(\mathbf{x})\rangle = \frac{\sum_{j=1}^{N} V_j f(\mathbf{x}_j) \nabla W(\mathbf{x}-\mathbf{x}_j; r_e)}{\sum_{j=1}^{N} V_j \nabla W(\mathbf{x}-\mathbf{x}_j; r_e)}. \tag{3.6}$$

Inconsistencies in derivative terms occur as well, but will not be corrected because of high computational cost and low sensitivity of the desired information to spatial derivatives (Liu et al., 2014). Therefore, Eqn. (3.6) may be used to calculate field functions, while Eqn. (3.5) may be used to calculate their derivatives.

With this formulation, the discrete set of particles, j, define f and its derivatives by carrying the function value at points $\mathbf{x}_j$. The value of f at $\mathbf{x}$ depends on the value of f assigned to particles within the influence radius, r_e, weighted by W, according to Eqn. (3.6). Equation (3.5) similarly defines the first derivative of the function, and by repeated application and substitution, higher order derivatives as well.

Traditionally, SPH has been used to solve complete physical problems in a Lagrangian sense. The LVOF approach uses these concepts to identify the location and geometry of fluid interfaces by applying SPH-inspired calculations to define the volume of fluid variable used in classical VOF. This process involves seeding the physical domain with phase-identifying particles. Properties calculated on (or carried by) these particles are then projected onto an Eulerian mesh, upon which the Navier-Stokes equations are solved by any standard approach.

The LVOF methodology has not appeared in the literature, but it will soon appear in a paper by Liu et al. (2014). A general review must therefore appear here, considering the unavailability of an external reference at present.[1] Some of the most intricate details are reserved for the forthcoming paper, but it is necessary to address the general methodology and some important implementation considerations.

3.1.2 Lagrangian volume of fluid

Consider a domain containing a single droplet and a uniform distribution of Lagrangian, phase-identifying particles, such that the inter-particle spacing is much smaller than the droplet radius, and smaller than the Eulerian mesh spacing. A

[1] The Ph.D. dissertation of Dr. Wanjiao Liu (Liu, 2014) is the origin of the method and serves as the only available reference.

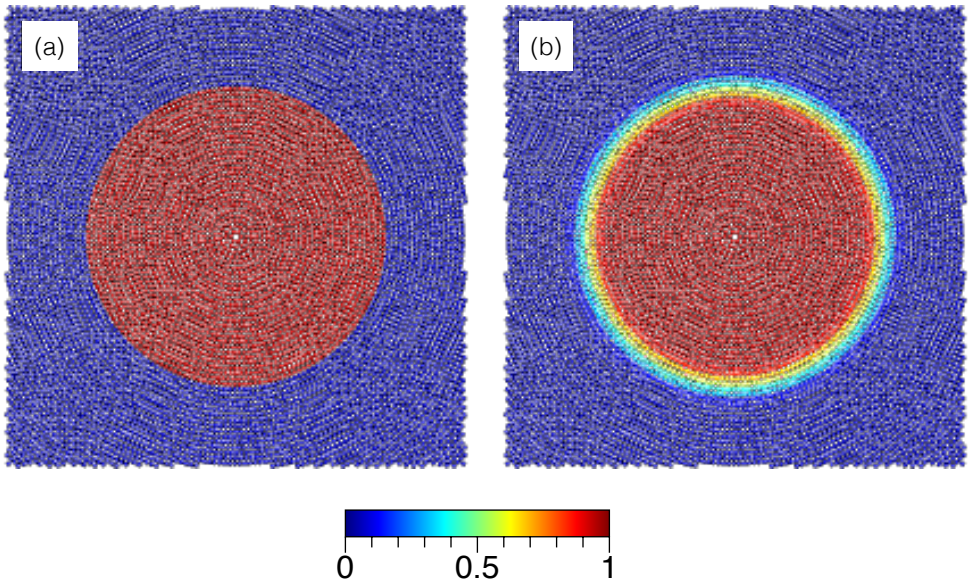

Figure 3.1. Lagrangian phase identities: (a) volume of fluid defined on particles; (b) color function calculated on particles.

domain of this kind appears in Figure 3.1(a). Particles inside the droplet carry a VOF value of 1, while the exterior particles carry a VOF value of 0. These intrinsic particle VOF values do not change with time, and forever define the two phases. The LVOF method seeks to characterize the droplet interface (location and shape) by using the local variation in VOF. Necessary and sufficient characterization of the interface includes identification of its normal and curvature.

Intuitively, the interface falls between two adjacent particles carrying different VOF values, but defining the interface discontinuously would generate numerical errors. For this reason, a new definition of the color function spreads the interface (over a surface in two dimensions, or a volume in three dimensions),

$$c_i = \frac{\sum_{j=1}^{N} \psi_j V_j W\left(\mathbf{x} - \mathbf{x}_j; r_e\right)}{\sum_{j=1}^{N} V_j W\left(\mathbf{x} - \mathbf{x}_j; r_e\right)}, \tag{3.7}$$

where ψ_j is the VOF of particle j (Liu et al., 2014). Rigorously, the color function

is simply a discrete kernel approximation of the VOF field. The color function corresponding to the VOF distribution in Figure 3.1(a) appears in Figure 3.1(b).

Because the color function approximates the VOF, the color function also assumes a magnitude of 1 in the dispersed phase and 0 in the continuous phase. Unlike the VOF, the color function presents a continuous gradient across the phase interface of thickness equal to twice the influence radius, r_e. In the transition region, the interface normal and color function gradient align (Morris, 2000),

$$\hat{n} = \frac{\nabla c}{|\nabla c|}, \tag{3.8}$$

and Eqns. (3.5), (3.7), and (3.8) allow for calculation of the unit-normal vector,

$$\hat{n}_i = \frac{\sum_{j=1}^{N} c_i V_j \nabla W\left(\mathbf{x} - \mathbf{x}_j; r_e\right)}{\left|\sum_{j=1}^{N} c_i V_j \nabla W\left(\mathbf{x} - \mathbf{x}_j; r_e\right)\right|}. \tag{3.9}$$

Finally, the interface curvature depends only on the unit interface normal,

$$\kappa = -\nabla \cdot \hat{n}. \tag{3.10}$$

Discretely,

$$\kappa_i = \sum_{j=1}^{N} \nabla W\left(|\mathbf{x}_j - \mathbf{x}_i|\right) \cdot \hat{n}_i V_j. \tag{3.11}$$

Although the general approach may be clear, some important intricacies must be considered: particle seeding, the weight function, the influence radius, and treatment of particles that carry improper normal vectors.

The radial seeding used in Figures 3.1(a) and (b) has important significance. When considering the influence radius and the weighting of particles, random or cartesian initializations unnecessarily introduce error. Errors become small when the particle resolution greatly exceeds the Eulerian mesh resolution and when the

influence radius is large. However, best-practice requires a radial initialization, assuming an influence radius of a few mesh spacings.

Following the methodology of Liu et al. (2014), the weight function of choice assumes the form,

$$W(r) = A \begin{cases} e^{-A\frac{r}{r_e}} - e^{-A} & r < r_e \\ 0 & r \geq r_e, \end{cases} \tag{3.12}$$

where

$$r = |\mathbf{x}_j - \mathbf{x}_i| \,. \tag{3.13}$$

The coefficient A ensures that W satisfies all of the requirements of a proper weight function. For a two-dimensional domain,

$$A = \left(2\pi r_e^2 \left[\frac{1}{c^2} - \left(\frac{1}{c^2} + \frac{1}{c} + \frac{1}{2} \right) e^{-c} \right] \right)^{-1} \tag{3.14}$$

and

$$c = 0.01 \tag{3.15}$$

satisfy the requirements.

This weight function has been adopted because other forms put too much weight on nearby particles, complicating the calculation of curvature and by extension surface tension (Liu et al., 2014). The quality of the curvature calculation also depends on the influence radius and the number of particles per Eulerian cell, referred to as the particle number density, ρ_p.

The Lagrangian curvature field associated with a unit radius droplet appears in Figures 3.2(a)-(d). Each of these figures displays a different configuration of influence radius, r_e, and Lagrangian particle number density, ρ_p. The radius of curvature carried by the particles should decrease as r^{-1} from the center of the droplet and have no angular dependency. Figures 3.2(a)-(c) show the quality of the

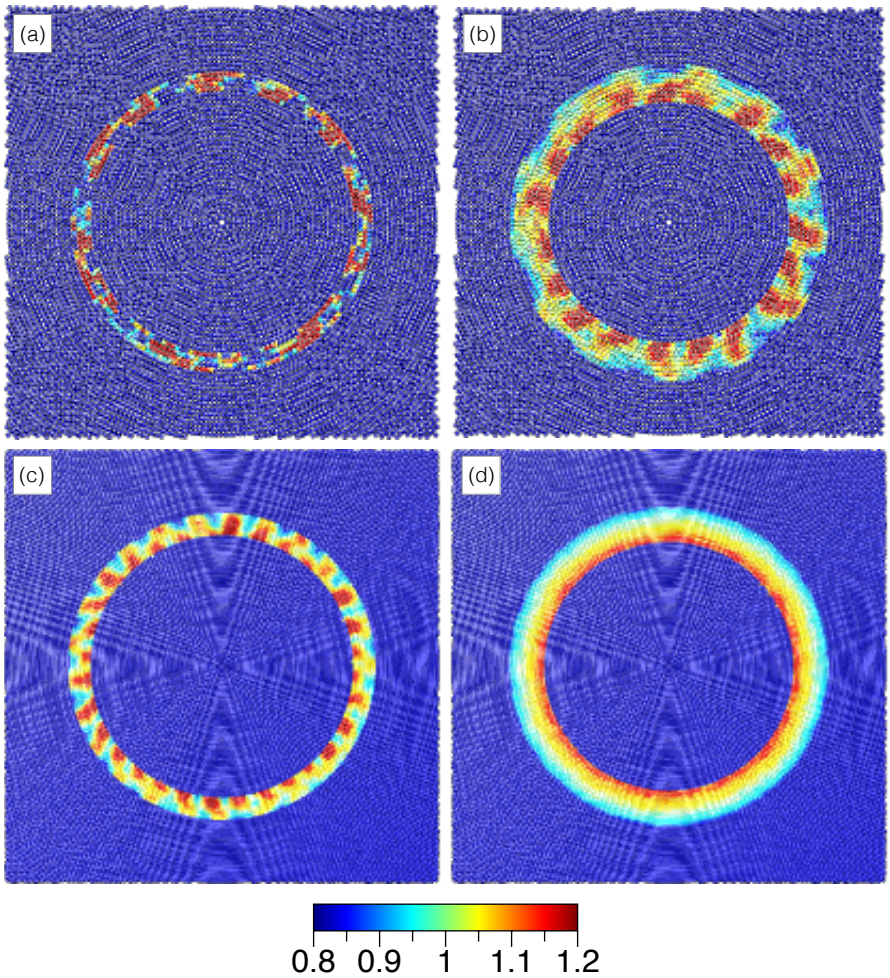

Figure 3.2. Curvature fields calculated with various r_e and ρ_p: (a) $r_e = 2dx$, $\rho_p = 2$; (b) $r_e = 3dx$, $\rho_p = 2$; (c) $r_e = 2dx$, $\rho_p = 10$; (d) $r_e = 3dx$, $\rho_p = 10$.

curvature calculation to become poor if either the particle number density or the influence radius becomes too small. Only with sufficiently high particle number density and sufficiently large influence radius does the curvature become accurate, as in Figure 3.2(d). Potential decreases in particle number density associated with flow shear further increase the importance of maintaining sufficient particle number densities. Numerical experimentation has shown particle number densities of 20 and an influence radius of three mesh spacings to be sufficient for the present

effort.

Improper curvature values may result despite a sufficient influence radius and high particle number densities. Morris (2000) attributes this behavior to particles that carry normal vectors that are too short to numerically resolve. To account for these poorly defined normal vectors, a Heavyside filter has been implemented so only particles carrying normal vectors greater than $0.01dx$ influence curvature. The remaining question is how these geometric factors may be used to inform the multiphase Navier-Stokes equations.

3.2 Fluid property and surface tension implementation

Fundamental to the communication between the particles and the Eulerian mesh is a shared coordinate system. A particle seeded at some location, $\mathbf{x}_i$, carries information relevant to the Eulerian mesh at the same location. Identifying all of the particles within a Eulerian cell and averaging their properties allows for the transfer of information from the Lagrangian particles to the Eulerian mesh. Similarly, interpolation of velocities at Eulerian nodes to the position of Lagrangian particles allows for the calculation of particle velocity, and the time integration of particle location. Determination of fluid properties and surface tension requires this communication.

A variable equivalent to the color function used in the VOF method can be generated by transferring the averaged Lagrangian color function to the Eulerian mesh. Fluid properties may then be defined with respect to this mean color function, ψ_c, in a way identical to Eqn. (2.5). For smooth (numerically differentiable) initialization of fluid properties, a sufficiently large influence radius (three mesh

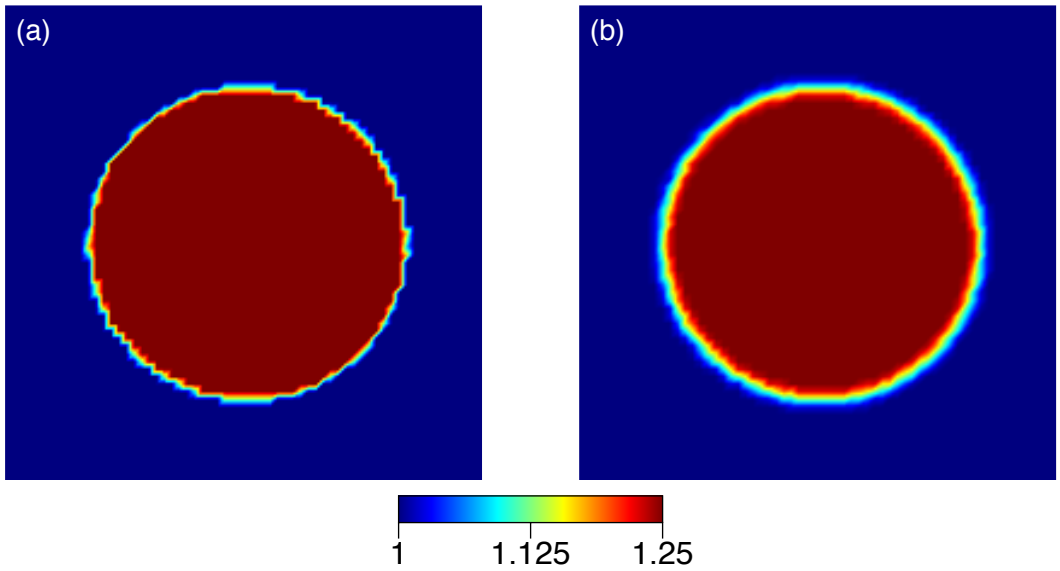

Figure 3.3. Pressure initializations: (a) discontinuous initialization based on the mean volume of fluid; (b) smooth initialization based on the mean color function.

spacings for our purposes) must be used. Figure 3.3(a) presents an initial droplet pressure field based on the mean volume of fluid, whereas Figure 3.3(b) presents the initialization based on the mean color function. Initialization based on the mean color function results in a smooth transition between the continuous and dispersed phase pressures, whereas initialization based on the mean volume of fluid does not. Expression of surface tension in the Eulerian sense also requires communication between the Lagrangian and Eulerian domains.

Multiple approaches for simulation of surface tension are possible. One may expect to use a continuum surface force (CSF) model, as in many historical simulations (Brackbill et al., 1992), but the presence of the Lagrangian particles suggests an SPH-based surface tension approach.

Surface tension has been calculated in an SPH environment by Morris (2000),

where the interparticle force due to surface tension is given by

$$(\mathbf{F}_{st})_i = -\sigma\kappa_i\mathbf{n}_i. \tag{3.16}$$

The individual particle forces are, once again, volume averaged and transferred to the Eulerian mesh for time advancement. Instead of appearing as a surface force, the surface tension becomes a volume force (in three dimensions). This is a general concept associated with the CSF model but it has been implemented from an SPH perspective. For this implementation to present accurate dynamics, the volume over which the surface tension appears must be small compared to the volume of the droplet. The surface tension volume force appears as a source term in the Eulerian solver.

3.3 Eulerian solver

The Eulerian solver has been provided by the Computational Transport Phenomena Laboratory at the University of Minnesota. It implements a second order accurate in time, fourth order accurate in space, explicit MacCormack method (Hoffmann and Chiang, 1989) to solve the conservative form of the compressible Navier-Stokes equations given by Eqns. (3.17-3.22), where all variables are nondimensional.

$$\frac{\partial\mathbf{U}}{\partial t} + \frac{\partial\mathbf{E}}{\partial x} + \frac{\partial\mathbf{F}}{\partial y} = \mathbf{H} \tag{3.17}$$

$$\mathbf{U} = \begin{bmatrix} \rho \\ \rho u \\ \rho v \\ T \end{bmatrix} \tag{3.18}$$

$$\mathbf{E} = \begin{bmatrix} \rho u \\ \rho u^2 + P - \tau_{xx} \\ \rho uv - \tau_{xy} \\ uT - \frac{1}{RePr}\frac{\partial T}{\partial x} \end{bmatrix} \tag{3.19}$$

$$\mathbf{F} = \begin{bmatrix} \rho v \\ \rho uv - \tau_{xy} \\ \rho v^2 + P - \tau_{yy} \\ vT - \frac{1}{RePr}\frac{\partial T}{\partial y} \end{bmatrix} \tag{3.20}$$

$$\mathbf{H} = -\frac{1}{We}\frac{\sum_{i=1}^{N} \kappa_i \mathbf{n}_i . V_i}{\sum_{i=1}^{N} V_i} \tag{3.21}$$

$$\tau_{ij} = \frac{1}{Re}\begin{bmatrix} \frac{2}{3}\left(2\frac{\partial u}{\partial x} - \frac{\partial v}{\partial y}\right) & \left(\frac{\partial u}{\partial y} + \frac{\partial v}{\partial x}\right) \\ \left(\frac{\partial u}{\partial y} + \frac{\partial v}{\partial x}\right) & \frac{2}{3}\left(2\frac{\partial v}{\partial y} - \frac{\partial u}{\partial x}\right) \end{bmatrix}. \tag{3.22}$$

The energy equation has been neglected by setting the temperature uniformly equal to one (isothermal). A passive scalar temperature, T, has been introduced to decouple the momentum and energy equations to better emulate an incompressible system. Modification of the equation of state is also necessary.

A stiffened equation of state is required to approximate an incompressible system. Simple stiffened equations simply use a stiffening pressure, P_s, to reduce the percent change in density associated with a given change in pressure (Abgrall

and Karni, 2000),

$$P = \rho RT - P_s. \tag{3.23}$$

This simplistic approach does not allow for control of the sound speed, and achieving a stable time step may be difficult. Instead, a Taits equation of state will be used (Sirotkin and Yoh, 2012),

$$P = \rho_0 \frac{c_s^2}{\gamma} \left[\left(\frac{\rho}{\rho_0} \right)^{\gamma} - 1 \right], \tag{3.24}$$

which allows for control of the speed of sound, c_s. For the purposes of this study, the parameters are selected such that

$$\rho_0 \frac{c_s^2}{\gamma} = 50.0$$

and

$$\gamma = 2.0.$$

The same equation of state may be used for both phases, allowing Eqn. (3.24) to apply throughout the domain.

The dimensionless density field may be initialized by considering Eqns. (3.24) and (2.26). After proper scaling, the initialization of density becomes

$$\rho = (1 - \psi_c) + \sqrt{\left(\frac{1}{50We} + 1 \right)} (\psi_c), \tag{3.25}$$

with the characteristic length taken as the droplet radius.

Initialization of pressure, and all successive pressure calculations, may be performed by means of Eqn. (3.24). When properly non-dimensionalized,

$$P = 50(\rho^2 - 1). \tag{3.26}$$

This formulation readily implements phase dependent properties and effectively decouples the energy and momentum equations.

3.4 Calculation of interfacial flux

Accurate calculation of interfacial fluxes requires a delicate compromise between interface thickness and accurate numerical differentiation. Properties change discontinuously across phase interfaces in the macroscopic physical world, but solving the physics from this perspective requires a jump condition at the interface most simply applied in a fully Lagrangian formulation. The LVOF method incorporates an interface of finite thickness across which properties vary and surface tension appears. The thickness of this region requires careful consideration.

The numerical derivatives of properties near the interface become inaccurate as the interface thickness approaches zero. Meanwhile, if the interface thickness becomes significant relative to the interfacial characteristic length, the physics become poorly represented. The nature of property variation also influences the accuracy of the flux calculation; potential error in flux calculation does not significantly influence the solution if properties do not vary appreciably across the interface. Significant pressure and density variations may occur across the interface of a low Weber number droplet, and therefore an exploration of this behavior is appropriate prior to result generation. These errors may be explored by considering the uniform advection of a droplet and observing the change in particle number density near the interface. Ideally, the particle number density should remain constant, but errors in interfacial fluxes promote variation.

Figure 3.4(a) and (b) display the particle number density in a domain with uniform velocity and a single low Weber number droplet ($We = 0.125$). In Figure

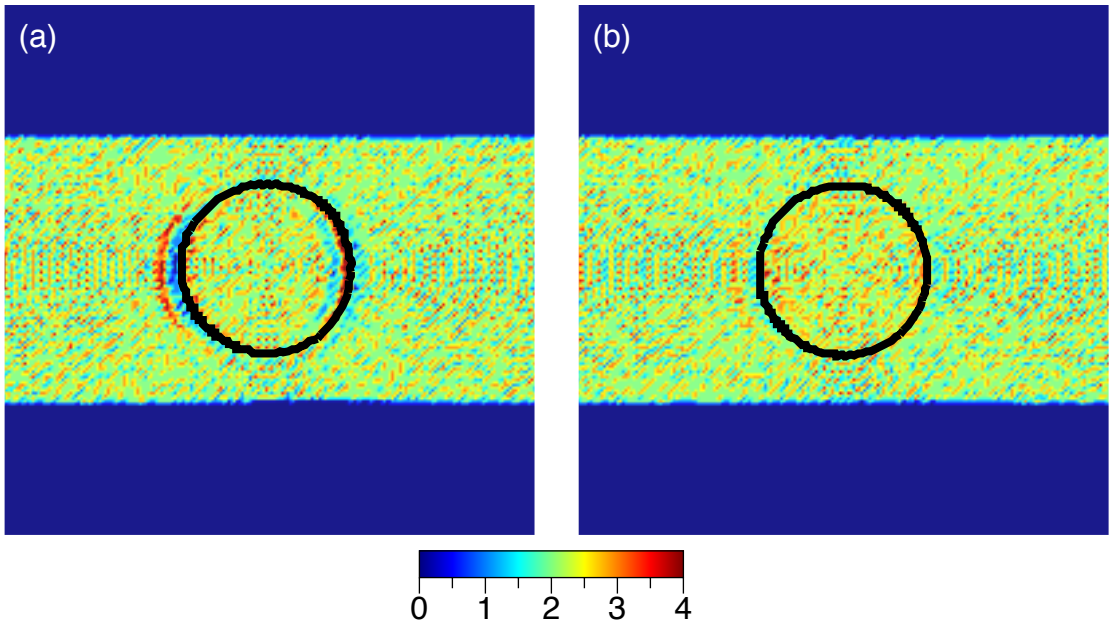

Figure 3.4. Particle number density variations due to inaccurate evaluation of interfacial flux: (a) $r_e = 2dx$; (b) $r_e = 4dx$.

3.4(a), $r_e = 2dx$, and in Figure 3.4(b), $r_e = 4dx$, and in both images the droplet has traveled three times its diameter. Numerical differentiation of density and pressure becomes inaccurate when the influence radius is too small (Figure 3.4(a)), resulting in particle number density variations near the interface. Conversely, flux calculations become more accurate and the particle density remains nearly constant with a thicker interface, as in Figure 3.4(b). The results in Figure 3.4 have been produced with a continuous to dispersed phase density ratio of 0.735, which naturally follows from the global equation of state and the low Weber number. This density ratio is significant and undesirable for the present efforts, and the percent error associated with flux calculations is significant. The equation of state must be used to reduce the density ratio and reduce flux errors (which results in the stiffened parameters described in Section 3.3).

Figure 3.5(a) shows the default equation of state with an influence radius

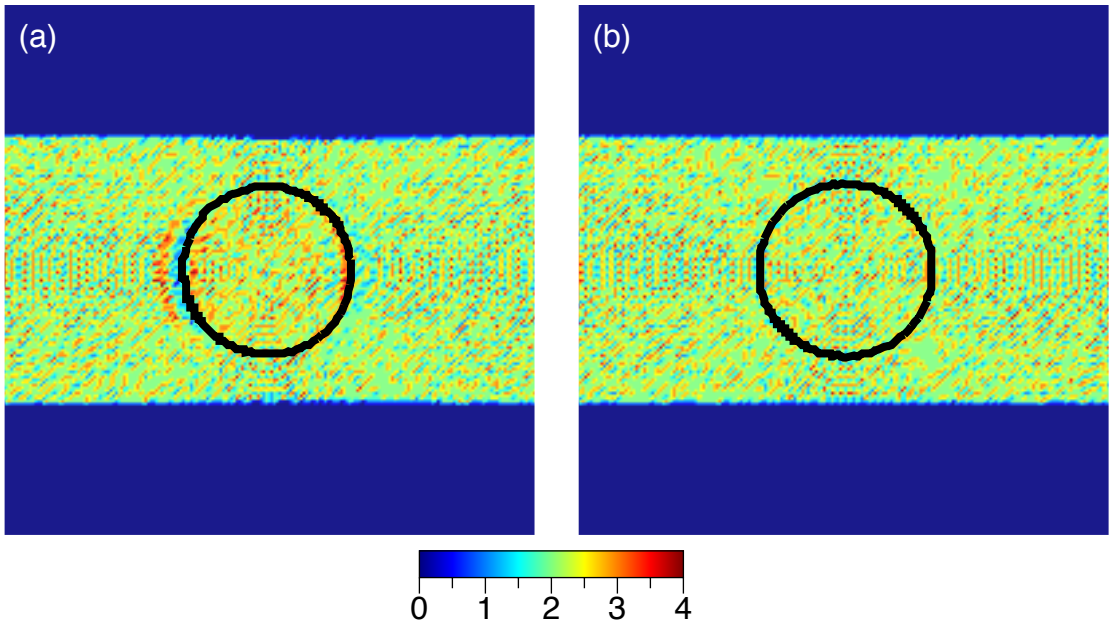

Figure 3.5. Improvement of interfacial flux evaluation by stiffening the equation of state at $r_e = 3dx$: (a) default equation of state; (b) stiffened equation of state.

of $3dx$, while Figure 3.5(b) shows the stiffened equation of state with the same influence radius. Reducing the property variation to less than five percent greatly increases the accuracy of the calculation, as evidenced by the uniform particle number density maintained in Figure 3.5(b). All future calculations utilize the stiffened equation of state.

Having developed a general understanding of the method, a sample problem serves as proof of the validity of the method, as well as adherence of the computer code to the method.

3.5 Verification

Validation of the method and solver is performed by observing the oscillation period of a $We = 1$ droplet (Liu et al., 2014). The analytical period of oscillation

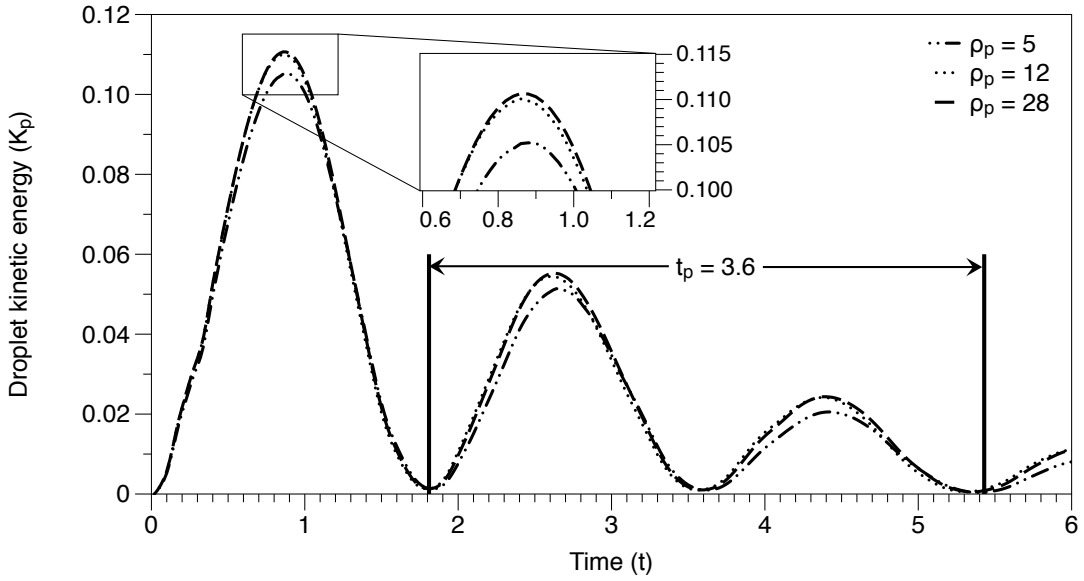

Figure 3.6. Oscillations of droplet kinetic energy, K_p, observed in the transition from elliptical to circular shape.

for an inviscid, initially elliptical droplet is $t_p = 3.63$ (normalized by the capillary time scale), and the oscillation period of droplet kinetic energy, K_d, is half the droplet oscillation period. The droplet kinetic energy presented in Figure 3.6 shows the calibrated oscillation period to be $t_p = 3.6$ when $Re = 25$, a close match to the analytical $t_p = 3.63$. Additionally, good convergence is observed for the $\rho_p = 12$ and $\rho_p = 28$ cases, suggesting $\rho_p = 12$ to be a sufficient particle number density.

The computations presented in the following chapter have been generated on a 256×192 mesh (43 nodes across the droplet). Increasing the mesh resolution by 25% to 320×240 (53 nodes across the droplet) results in less than 0.5% change in volume averaged droplet temperature for $Re = 5$ and $We = 0.5$, run until $t = 5$. The small change suggests that the 256×192 grid is sufficient for the low Reynolds numbers explored here.

Chapter 4

Results

In an effort to reduce the full problem to its simpler components, results appear in a series of sections of increasing physical complexity. Results for conduction heat transfer appear first, followed by the hydrodynamic problem, and finally the fully coupled thermal and hydrodynamic problem.

4.1 Conduction heat transfer

Spatial variations in Prandtl number produce regions of relatively high and low thermal resistance, and modify the temperature field compared to the uniform Prandtl number case. A basic exploration of this behavior must be performed prior to solving the fully coupled problem to isolate behaviors attributable to property variation alone. The conduction problem serves as a suitable platform for this exploration.

The initial temperature field defined by Eqn. (2.22) appears in Figure 4.1(a). Setting the continuous phase Prandtl number and Reynolds number equal to one and the temperature gradient at the lower boundary equal to -1.5 produces a

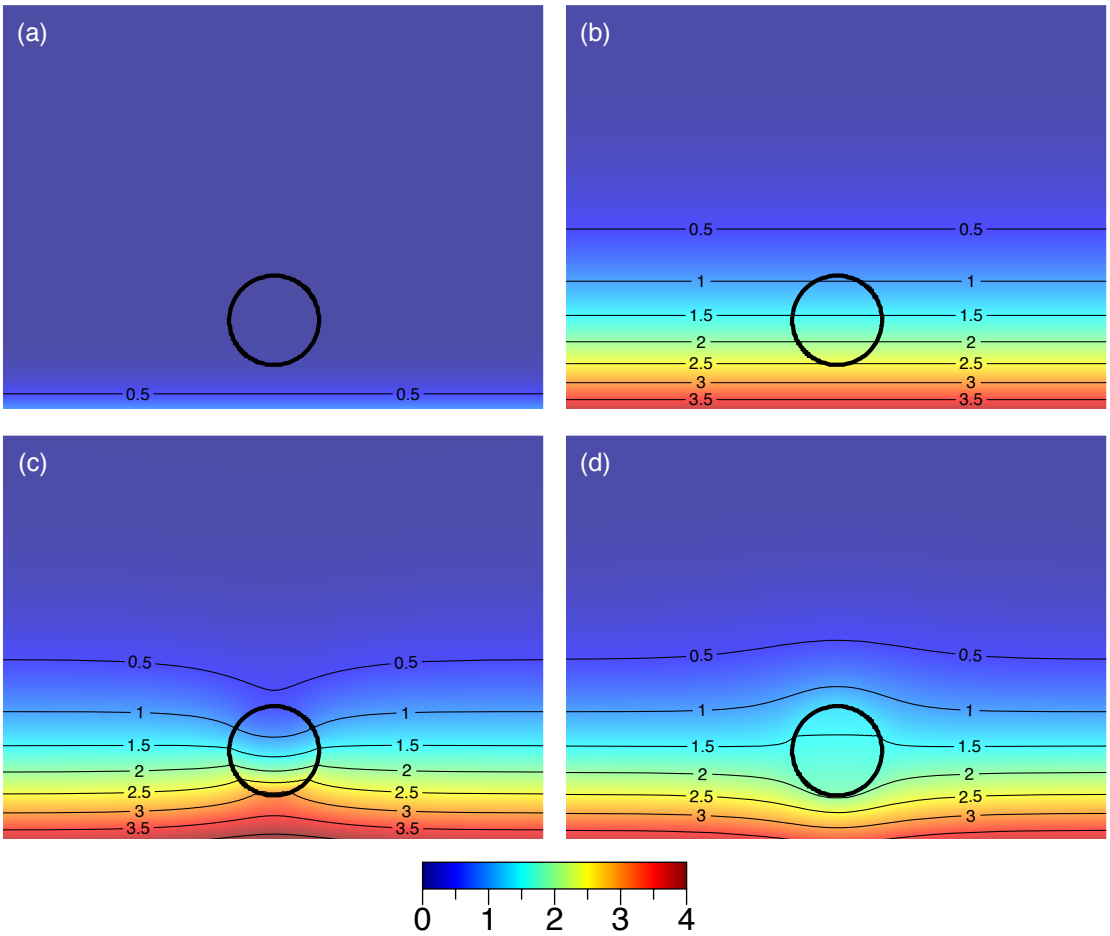

Figure 4.1. Conductive temperature (T) fields: (a) $t = 0$; (b) $Pr_d = 1$, $t = 5$; (c) $Pr_d = 5$, $t = 5$; (d) $Pr_d = 0.2$, $t = 5$.

constant heat flux boundary condition. Temperature fields at $t = 5$ for Pr_d equal to 1, 5, and 0.2 appear in in Figues 4.1(b)-(d), respectively.

Figure 4.1(b) displays the simplest case, with the Prandtl number globally set equal to one (hereafter referred to as the uniform case). The phase interface, identified by the black circle, does not modify the one-dimensional thermal boundary layer evolution, as expected. This case has been presented simply to inform temperature variations attributable to surface tension induced vorticity in later

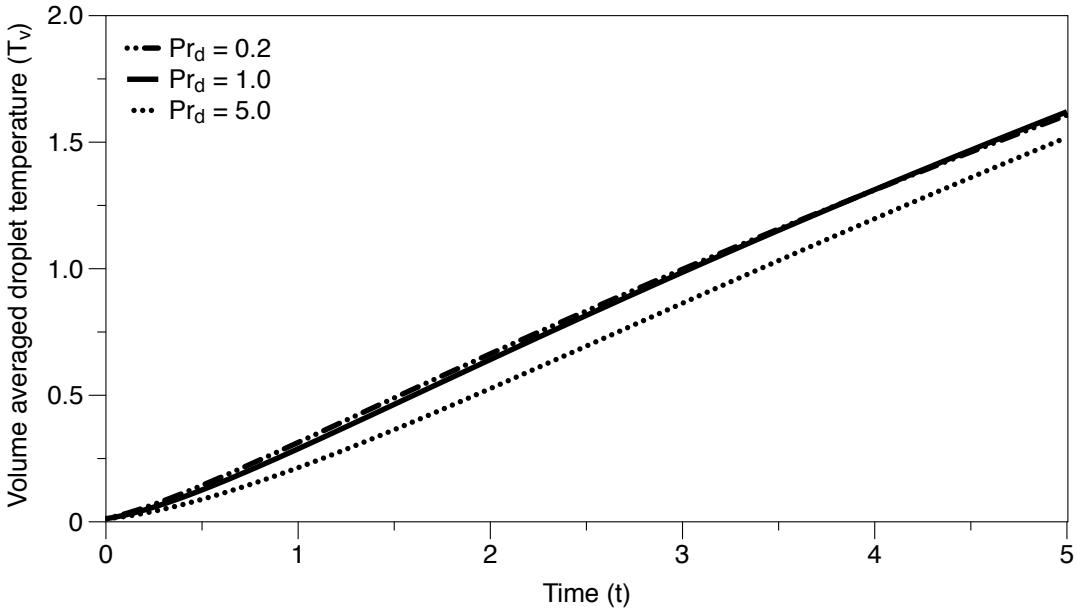

Figure 4.2. Volume averaged droplet temperature as a function of Pr_d in a conductive environment.

sections. More interesting results appear in Figures 4.1(c) and (d), which present the high and low Biot number cases, respectively.

In adherence to the general assumption of noninteractive dispersed phases in dilute systems (Michaelides, 2006), perturbations to the thermal boundary layer only propagate a few radii from the droplet surface. Variations in thermal resistance near the constant heat flux boundary generate local temperature plateaus in the case of low Prandtl number droplets and depressions in the case of high Prandtl number droplets. The maximum temperature in the high Biot number droplet ($T \sim 3$) significantly exceeds that of the low Biot number droplet ($T \sim 2$), partially because of the difference in Prandtl number, but also because of the difference in local maximum temperature due to the surface proximity. The higher maximum temperature in the high Biot number case has clear significance in boiling applications, but the volume averaged temperature is also important,

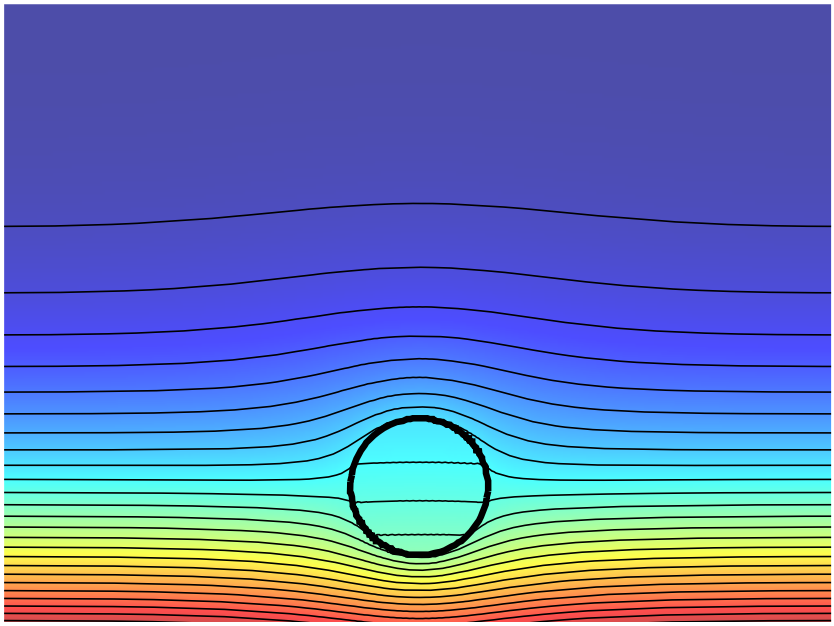

Figure 4.3. High resolution temperature (T) contours (same color scale as Figure 4.1). $Pr_d = 0.2$.

and appears as a function of time in Figure 4.2.

Despite a lower maximum temperature, the low Biot number droplet always presents a greater volume averaged temperature, T_v, which roughly equals that of the uniform Prandtl number case. The small difference between the two, particularly prominent at early times, is believed to be caused by the nonuniform initial droplet temperature (the initial volume averaged droplet temperature is approximately 0.013, rather than 0.0). At $t = 5$, the difference between the $Pr_d = 0.2$ and $Pr_d = 1$ cases is 0.8%, which may be attributable to the averaging method, the interface thickness, or mild under-resolution. The general heating tendencies may be qualitatively understood by observing Figures 4.1(b)-(d).

In the high Biot number droplet, the temperature distribution displays a concave shape due to bulk energy transfer in the positive y direction. This bias

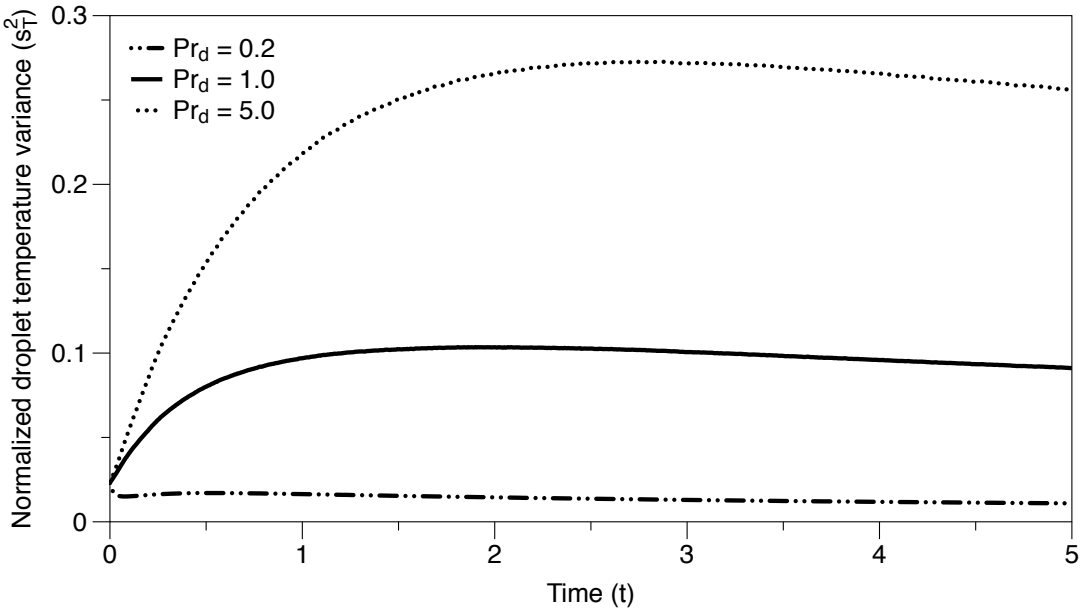

Figure 4.4. Droplet temperature variance normalized by T_v.

generates a volume averaged temperature that temporally lags that of the uniform Prandtl number and low Biot number cases, which display zero curvature in their (internal) temperature distributions. A high resolution image of the low Biot number case appears in Figure 4.3 (the contour labels have been omitted for clarity), where the internal droplet temperature distribution displays a one-dimensional character. Low Biot number droplets display this characteristic because any build up of thermal energy quickly transfers to a different surface of lower temperature, resulting in a net zero departure from the uniform Prandtl number case with respect to volume averaged temperature.

Differences between high and low Biot number droplet temperature distributions arise quantitatively in the droplet temperature variance normalized by the

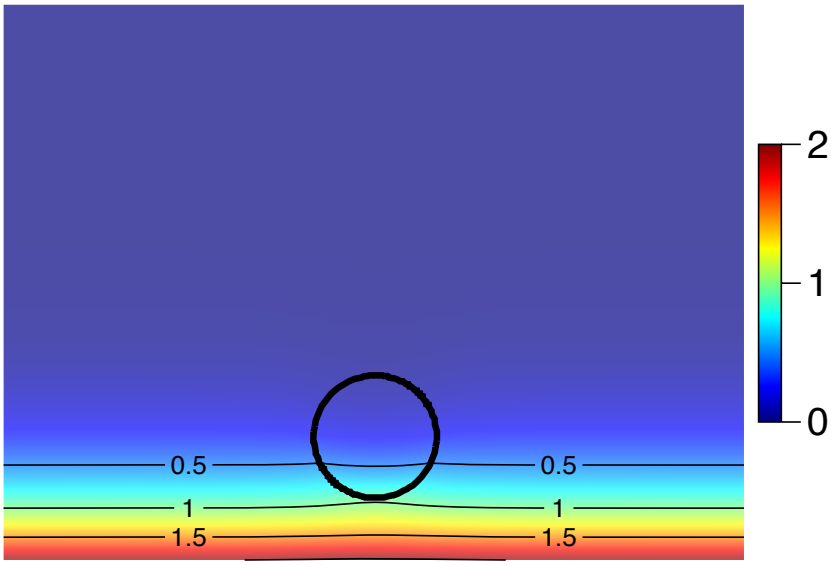

Figure 4.5. Temperature (T) contours for FC-72 ($Pr \sim 12.0$) in water ($Pr \sim 7.0$).

volume averaged droplet temperature,

$$s_T^2 = \frac{\sum_{j=1}^{N} (V_i \psi_i T_i - V_i \psi_i T_v)^2}{\sum_{j=1}^{N} V_i \psi_i T_v}, \tag{4.1}$$

which appears in Figure 4.4. All of the cases present a local maximum that results from the development of the droplet temperature distribution. As the dispersed phase Prandtl number increases, the time required to achieve the droplet temperature distribution increases, and therefore the time at which the maximum occurs increases with increasing Prandtl number. The non-zero y intercept indicates the non-uniform initial droplet temperature. As expected, the normalized temperature variance associated with the low Biot number droplet is an order of magnitude less than that of the high Biot number droplet. Convective mixing may accentuate these discrepancies.

A final observation is the presence of a transient heating regime, followed

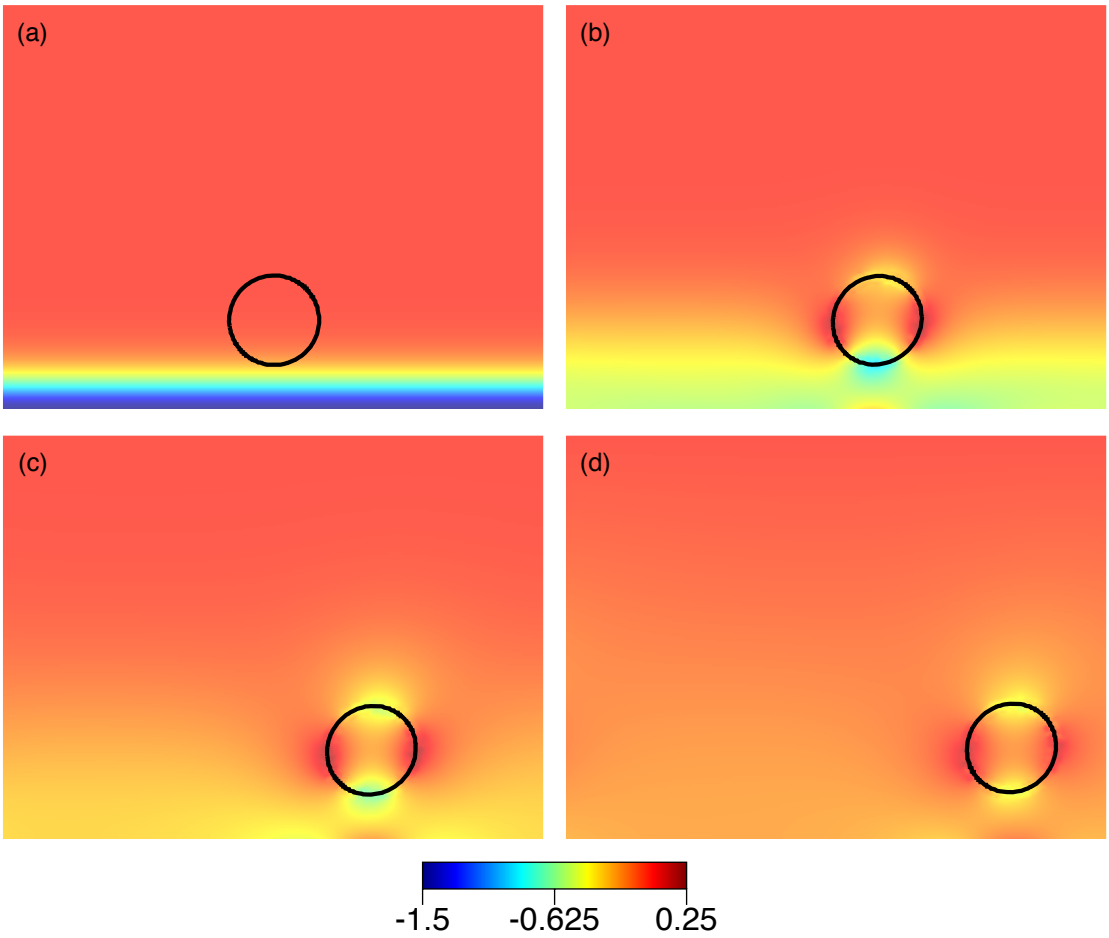

Figure 4.6. Instantaneous vorticity (ω) profiles for $Re = 1.0$ and $We = 0.5$ at: (a) $t = 0$; (b) $t = 1$; (c) $t = 3$; (c) $t = 7$.

by a steady heating rate which appears independent of dispersed phase Prandtl number. At a given time, the volume average temperature of a high Prandtl number dispersed phase is lower than that of a low Prandtl number dispersed phase, but the heating rates are equivalent. This may be perceived as the high Prandtl number droplet requiring a larger average temperature difference with the continuous phase to generate the same mean heating rate, which it achieves by an elongation of the transient heating regime. The Prandtl number ratios presented

here are fairly extreme, and a more realistic scenario reflecting FC-72 in water appears in Figure 4.5.

The Prandtl number ratio of FC-72 to water is near unity, resulting in little deformation of the boundary layer, which evolves at a slower rate than the previous cases because of the increase in continuous phase Prandtl number from 1.0 to 7.0. Introduction of convection may change some of these behaviors, suggesting it prudent to explore the nature of fluid motion independently of heat transfer.

4.2 Isolated hydrodynamic case

Low Weber number droplets tend to retain a near circular shape despite flow shear. In a boundary layer, this rigidity allows communication between relatively high and low velocity fluid and disrupts normal boundary layer development. Understanding this behavior prior to solving the full problem allows for general prediction of convective behaviors with the addition of heat transfer.

The vorticity field of a boundary layer at different times appears in Figure 4.6, where $We = 0.5$ and $Re = 1.0$. The droplet is nearly ridged, and it has been determined that further decreasing the Weber number has little influence on the solution. Early development of the boundary layer appears in Figure 4.6(b), where the droplet retains a near-circular shape and disrupts the boundary layer development. Similar to the conduction problem, the region of disruption remains relatively localized near $t = 0$. Eventually, near $t = 7$, the disruption region grows in size due to diffusion and the continuous reduction of velocity gradients. Disturbances propagate greater distances near the wall, which may result from low velocities and a lack of momentum in the near-wall region.

Increasing the Reynolds number to 5 has an expected influence on the solution,

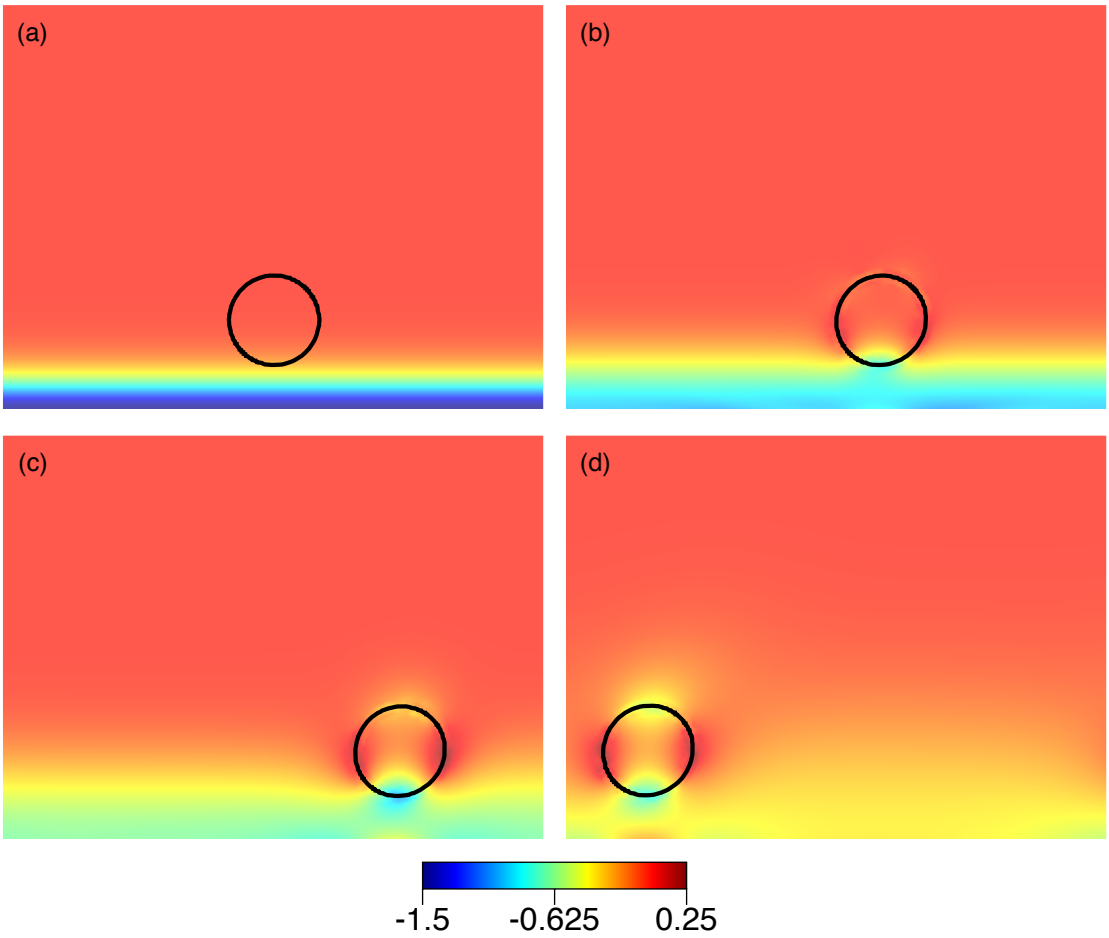

Figure 4.7. Instantaneous vorticity (ω) profiles for $Re = 5.0$ and $We = 0.5$ at: (a) $t = 0$; (b) $t = 1$; (c) $t = 3$; (c) $t = 10$.

as shown in Figure 4.7; the boundary layer develops more slowly in time, allowing advection to assume a more significant role. The vorticity generated inside the droplet serves as a mixing mechanism and a primary source of convection in the presence of heat transfer.

Relative velocity between fluid at the top and bottom of the droplet generates a clockwise spinning motion observable in the vertical velocity component shown in Figure 4.8(a). The rotation rate is roughly an order of magnitude less than

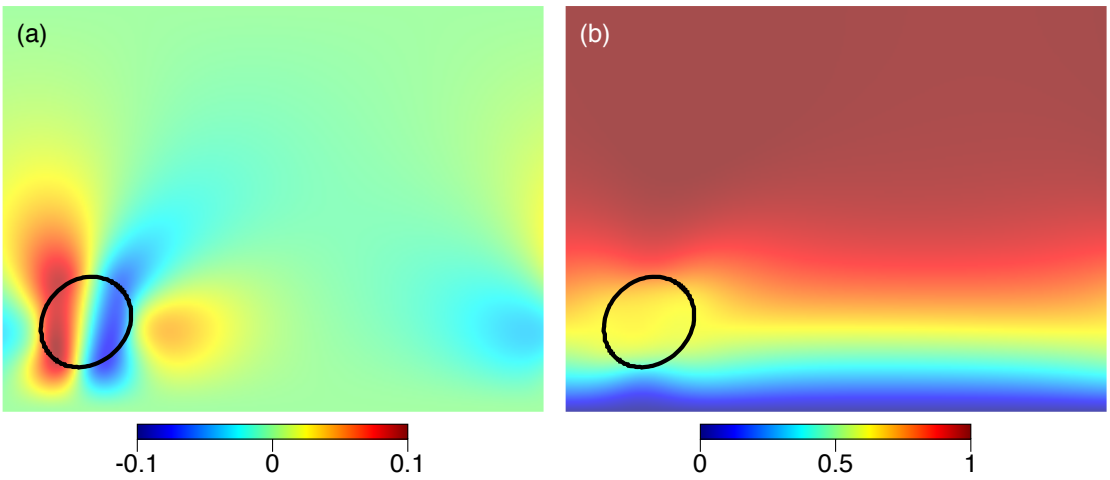

Figure 4.8. Velocity components for $Re = 5.0$ and $We = 1.5$: (a) vertical component, v; (b) horizontal component, u.

the gross advection speed, and therefore does not obviously present itself in the horizontal velocity component in Figure 4.8(b). Rotation is expected to have little influence on the droplet heating rate at the low Reynolds numbers explored here, but would become a significant mixing mechanism at large Reynolds numbers.

In the large Reynolds number regime where diffusion does not quickly smooth gradients, droplet rolling constitutes a mode of internal droplet circulation notably different from that observed in droplets placed in cross flow. Instead of two counter-rotating vortices inside the droplet, the droplet itself rotates relative to the continuos fluid, and a boundary layer structure appears to maintain velocity continuity.

Figures 4.8 and 4.9 show the tendency for increased deformation at increasing Weber numbers. In Figure 4.8 the Weber number is 1.5, and the droplet slightly departs from a circular shape. Further increasing the Weber number to 3, as in Figure 4.9(a), allows the droplet to obtain an oblong shape, and the $We = 5$ case in Figure 4.9(b) shows even more deformation and inclination. Displacement

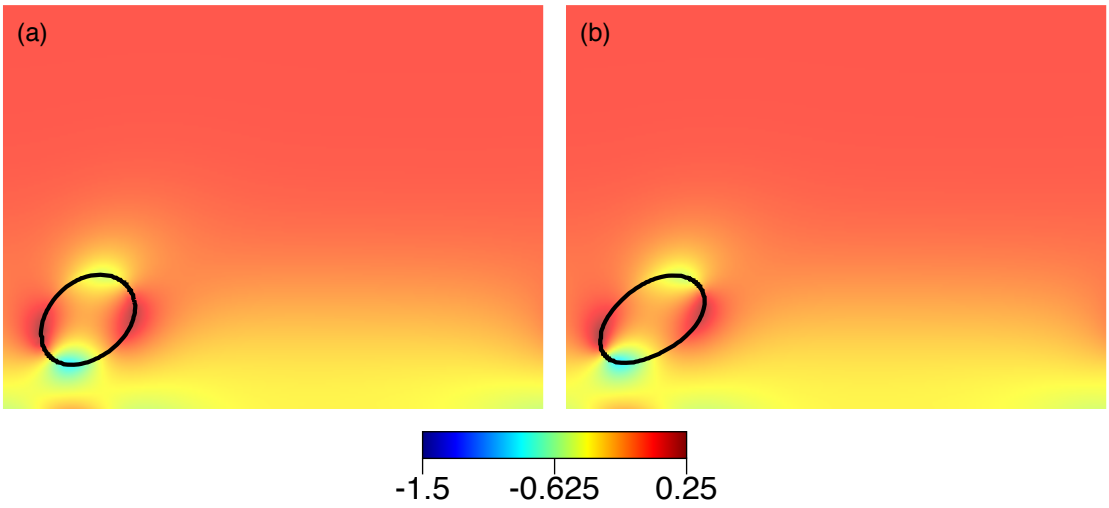

Figure 4.9. Interface deformation observed in the vorticity (ω) field at $Re = 5$ and: (a) $We = 3$; (b) $We = 5$.

of the droplet from the bottom surface due to the Magnus force does appear to a significant degree in any of the cases presented because of the short duration and the slow rotation rate compared to the characteristic velocity. Observation of significant Magnus force requires longer run times.

Measurable displacement due to the Magnus force appears in Figure 4.10, where the droplet location appears at times $t = 0$ and $t = 20$. Initially, the distance between the droplet and the wall (measured from the bottom of the droplet to the wall) is 1.0, but increases to 1.17, amounting to a 17% increase in wall/droplet separation distance. The droplet continues to rise in time, provided the continued presence of shear. With the introduction of heat transfer, this separation serves to distance the droplet from the heated surface, and is expected to reduce droplet heating rates.

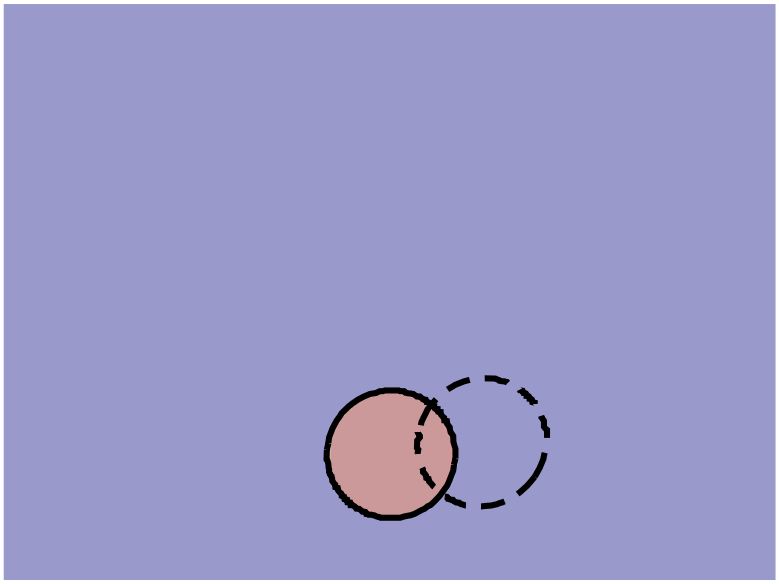

Figure 4.10. Displacement of the droplet from the lower surface by the Magnus force at $Re = 5$ and $We = 0.5$. Blue and red indicate the continuous and dispersed phases at $t = 0$, respectively. The dashed line denotes the phase interface at $t = 20$.

4.3 Coupled thermal/hydrodynamic case

To begin once more with the simplest case, the uniform Prandtl number condition ($Pr = 1$ in both phases) appears in Figure 4.11(a) for $Re = 1$ and Figure 4.11(b) for $Re = 5$. The vorticity generated by the droplet produces a clockwise swirling of the internal temperature distribution that is more prominent in the $Re = 5$ case, but does not appear to have a profound influence in the low Péclet number regime in general. A qualitative comparison of Figures 4.11 and 4.1(a) suggests the heating rate to be relatively unaffected by the inclusion of convection, and similar conclusions may be drawn about the high and low Biot number cases at $Re = 1$, appearing in Figure 4.12(a) and (b). Quantitatively, volume averaged temperature differences between the conduction and conduction plus convection

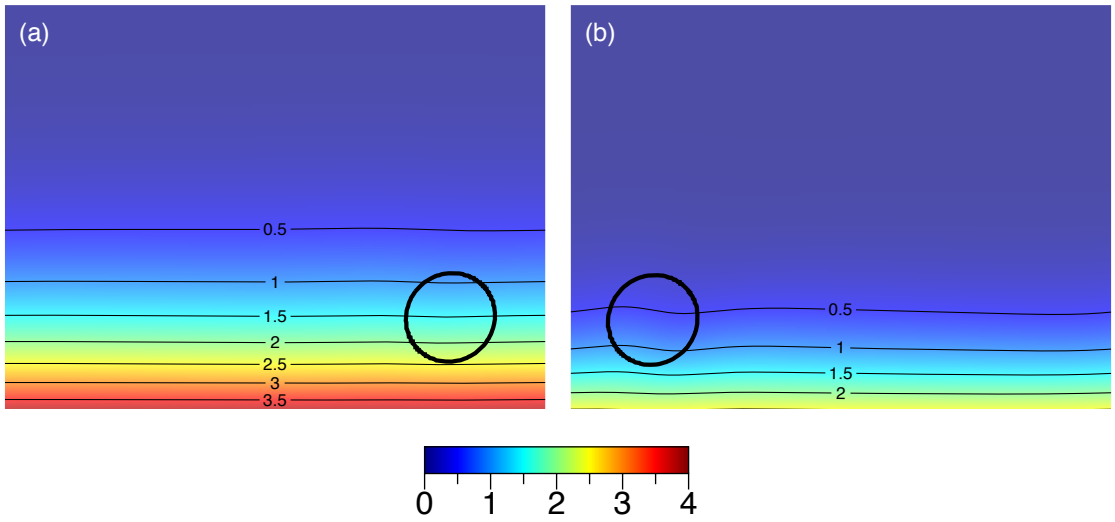

Figure 4.11. Temperature (T) fields for $Pr_d = 1$ and: (a) $Re = 1$, $t = 5$; (b) $Re = 5$, $t = 10$.

cases have been deemed negligible ($< 1\%$) for $Re = 1$, provided the Magnus force does not separate the droplet from the heated surface. Eventually, the Magnus force separates the droplet from the surface, and this heating similarity no longer applies.

Convective behavior is most prominent in the high Biot number droplet at $Re = 5$ (Figure 4.12(c)), where relatively cool fluid visibly travels from the top of the droplet along its leading surface because of droplet rolling. This internal convection cannot be observed in the low Biot number droplet for either Reynolds number because of high diffusivity (small Péclet numbers), but all cases present an asymmetric exterior temperature profile.

Although the droplet heating rates for conduction and convection cases are the same for early times, the droplet eventually displaces from the heated surface due to the Magnus force, as observed in Figure 4.10. Figure 4.13 shows the volume averaged temperature for the conduction, $We = 0.5$, and $We = 5.0$ cases at

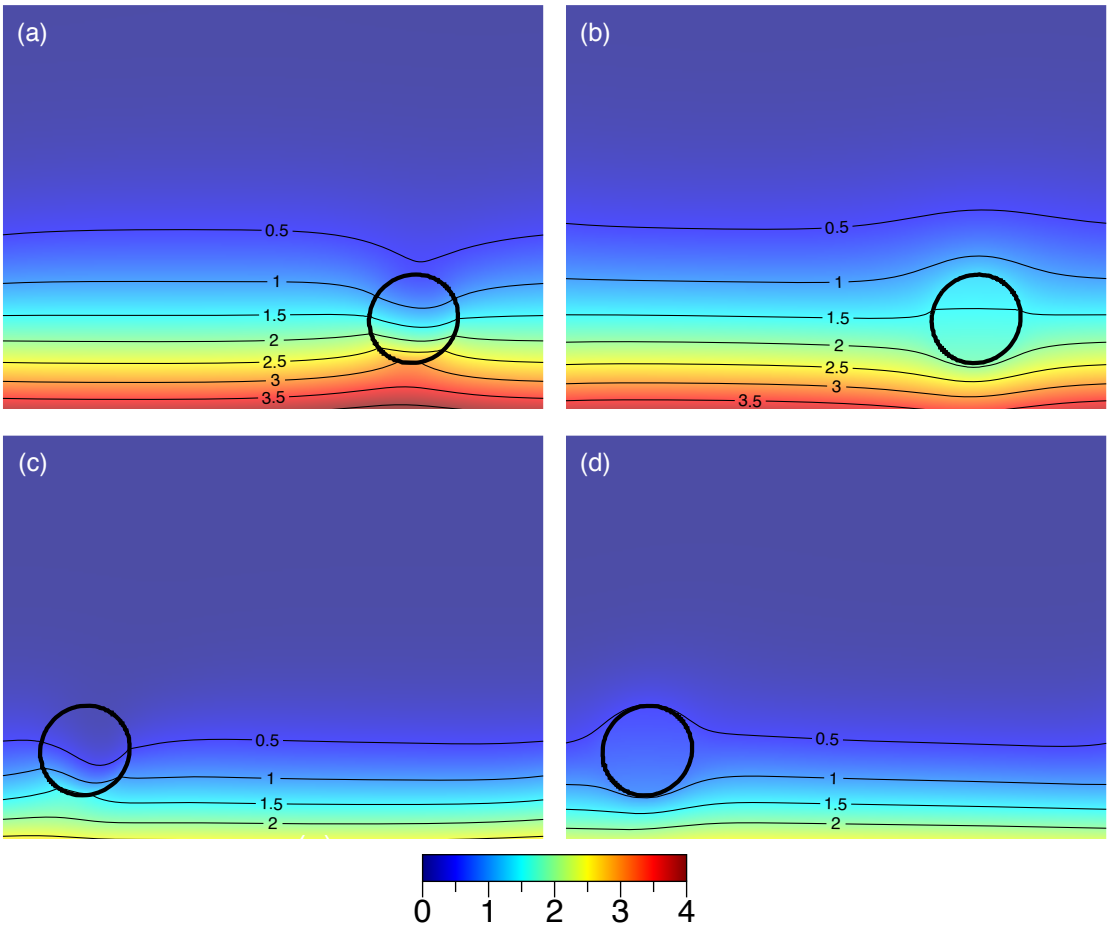

Figure 4.12. High and low Biot number temperature (T) fields: (a) $Pr_d = 5$, $Re = 1$, $t = 5$; (b) $Pr_d = 0.2$, $Re = 1$, $t = 5$; (C) $Pr_d = 5$, $Re = 5$, $t = 10$; (d) $Pr_d = 0.2$, $Re = 5$, $t = 10$.

$Re = 5$. A clear reduction in heating rate for the convective cases due to increased droplet/surface displacement occurs as time progresses. The more ridged droplet ($We = 0.5$) heats more quickly than the deformable droplet ($We = 5.0$), but the difference is small, and an obvious explanation does not present itself (it could be, perhaps, attributable to the difference in location of the droplet center of mass, or to small differences in mixing). In general, the volume averaged heating rate does not depend strongly on deformation, in agreement with Dai et al. (2002).

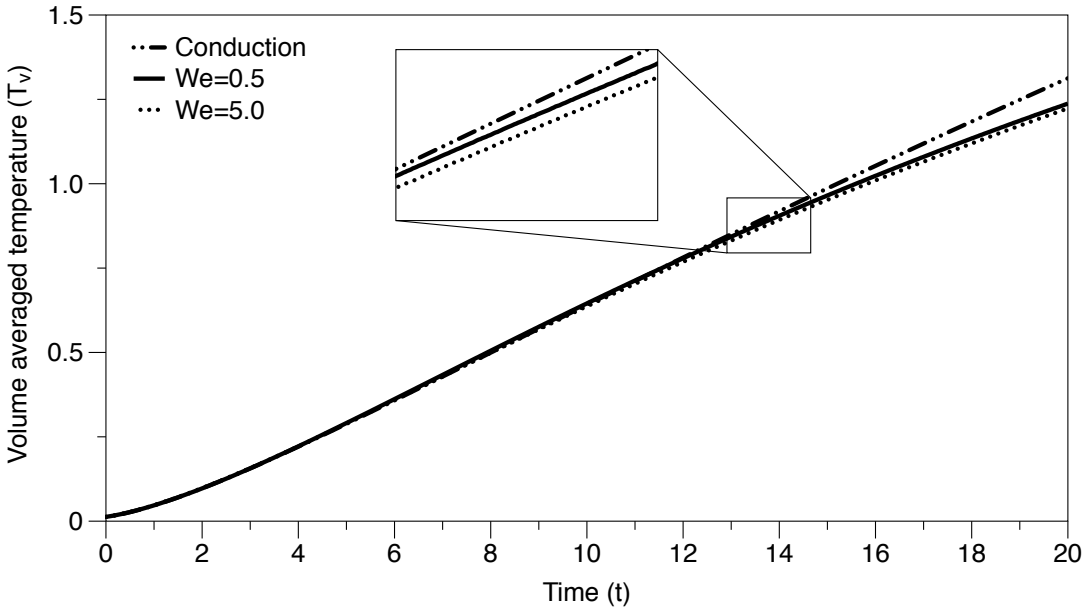

Figure 4.13. Influence of the Magnus force on droplet heating. $Re = 5$.

Chapter 5

Discussion

The results presented in Chapter 4 inspire a method for predicting the boiling entry length and physically inform dispersed phase modeling in Euler-Lagrange simulation of droplets in channel flow. This chapter expounds upon both of these topics.

5.1 The boiling entry length

The approach used to to generate the results in Chapter 4 does not allow for a robust prediction of the boiling entry length for real applications, but rather provides a means to observe the heating process, which allows for an informed simplification of the problem. A useful prediction of the boiling entry length may be constructed by coupling observations garnered from the simulations with the experimental results of Roesle (2010).

In measurements of dilute emulsion pool boiling (FC-72 in water), Roesle finds significant superheat is required to incite boiling. The saturation temperature of FC-72 is 56°C, but Figure 5.1 shows pool boiling not only requires approximately

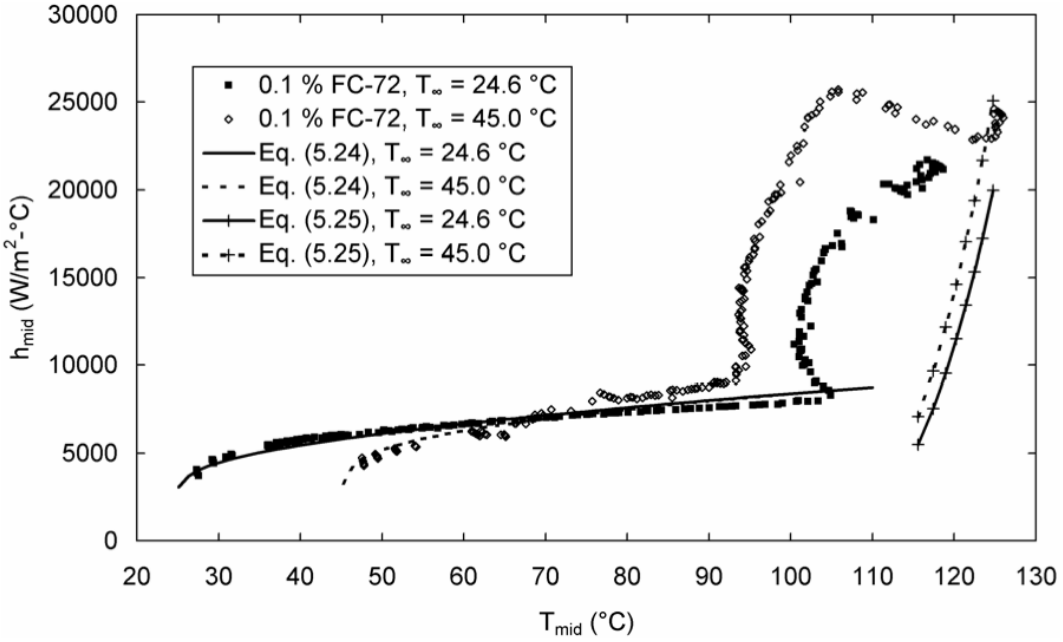

Figure 5.1. Heat transfer from a wire in pool boiling of a dilute FC-72 in water emulsion (Roesle, 2010).

50°C of super heat, but also depends on the farfield temperature.[1] Another notable feature of Figure 5.1 is the significant promotion of heat transfer at the onset of dispersed phase boiling. Harnessing this advantage for use in applications would be simplified by a method for predicting the boiling entry length; the results presented in Chapter 4 allow for the development of a first-level prediction tool.

Despite the intricacies of the cases described in Chapter 4, the temperature within the droplets does not depart significantly from the temperature of the boundary layer had the droplet been absent. Indeed the temperature distributions of each droplet may be different, but in a first analysis one may consider the boundary layer temperature without the droplet as a good prediction of the

[1] Figure 5.1 appears here without modification from the original source. The equation numbers, which reference standard fit equations, should be ignored, as they do not pertain to this thesis.

droplet temperature, particularly for dilute systems with dispersed to continuous phase Prandtl number ratios near one. The highly diffusive liquid/liquid near-wall region explored in this analysis allows for the temperature equivalency that is not observed in liquid/gas systems with high variability in Prandtl number and significant relative velocities (such as the problems historically solved with droplet heat transfer models). Changes in Prandtl number ratio, Reynolds number (provided the Reynolds number remains small), and Weber number do not significantly degrade the quality of the temperature equivalency assumption. As the Weber number increases and the Prandtl number ratio approaches unity, the quality of the assumption improves.

Coupling the assumption of droplet/continuous fluid temperature equality with known superheat requirements allows for prediction of the boiling entry length in microchannels with known temperature distributions. Superheat requirements for pool boiling have been presented, but the presence of nucleation sites in channel flow may eliminate a superheat requirement altogether. Future work must justify this claim. For now, a solution is sought to correlate a temperature rise (relative to the inlet temperature) to a travel distance along the heated surface.

The classical advection/diffusion problem in a tube provides a reasonable medium to demonstrate a solution based on the dispersed/continuous phase temperature equality assumption. One solution may be constructed by imposing a fully developed velocity profile and a constant surface heat flux; the former justified by the presence of an unheated starting length associated with transporting the fluid from a reservoir to the heated surface, and the latter justified by the nature of steady state electronic component heat dissipation with negligible end effects. Granted, real application does not identically satisfy either of

these assumptions, but this prediction of the boiling entry length serves to inform component design from a first level perspective.

Proper nondimensionalization of channel flow requires scaling both the streamwise and crosstream features to the same magnitude. The appropriate length scale for the axial direction accounts for diffusion,

$$z^* = 4\left(z/D\right)/\mathrm{RePr}, \tag{5.1}$$

where z is the axial displacement from the heated inlet, and D is the dimensional tube diameter. The radial direction scales by the tube radius. With these scalings,

$$\frac{T_w - T_0}{q_w R/k} = 2z^* + \frac{11}{24} + \sum_{n=1}^{\infty} C_n \exp\left(-\lambda_n^2 z^*/2\right) R_{1n}(1), \tag{5.2}$$

where C_n are the expansion constants , λ_n^2 are the eigenvalues, and $R_{1n}(1)$ are eigenfunctions, which may be retrieved from Burmeister (1993). The wall temperature rise, $T_w - T_0$, corresponds to the temperature rise of the most rapidly heated droplets as a function of z^*, assuming temperature continuity and the presence of droplets very near the wall. A parametric solution to Eqn. 5.2 is sought to describe z^* as a function of $q_w R/k$, to account for thermal boundary condition variations, as well as the temperature rise, $T_w - T_0$, to absorb the saturation temperature and the inlet coolant temperature. Reasonable ranges and magnitudes for these parameters follow from considering the fluid properties of water, the heat fluxes achieved in microchannels ($10 - 100\ W/cm^2$), and microchannel dimensions ($50 - 500\ \mu m$ in hydraulic diameter). The solution of Eqn. 5.2 encompassing this parameter space appears in Figure 5.2.

Knowing the inlet and saturation temperatures, Figure 5.2 may be used either to select the Reynolds number required to achieve a desired boiling entry length,

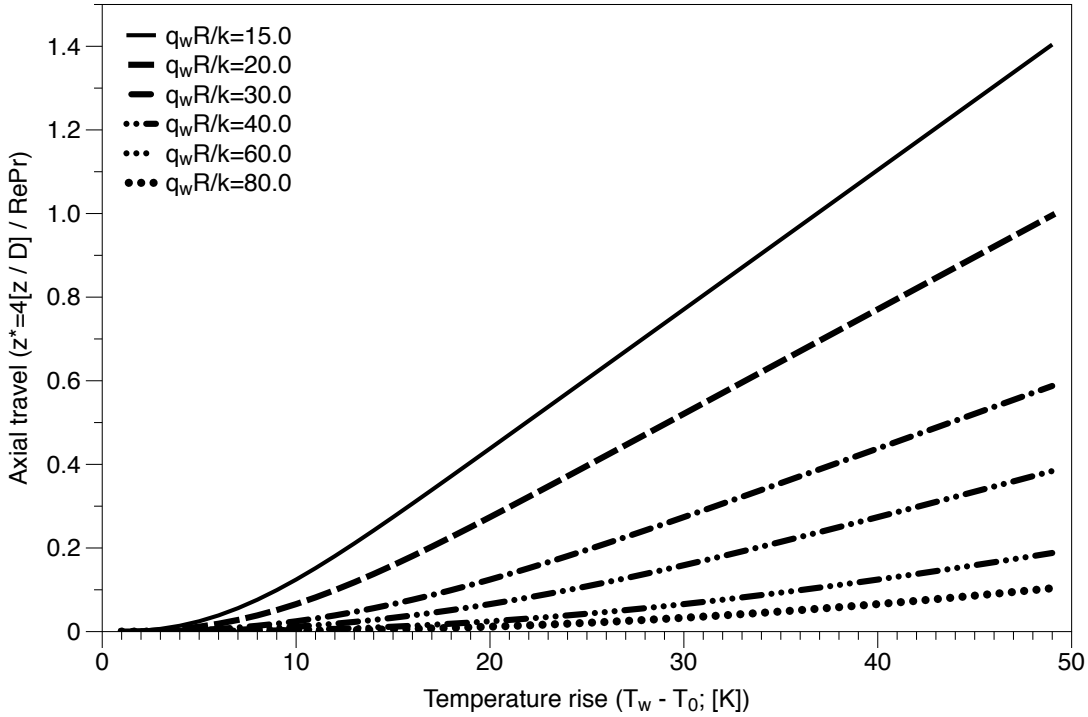

Figure 5.2. Boiling entry length in a round tube for fully developed flow and constant wall heat flux.

or to predict the boiling entry length associated with a given Reynolds number. The required travel distance, z, decreases with decreasing temperature rise and decreasing Péclet number for a fixed heating parameter. These relations are reasonable because lower Péclet numbers associate with dominant diffusion, and a greater temperature rise requires longer residency and increased travel.

As observed in the results of Chapter 4, a linear heating regime follows a nonlinear heating regime of duration controlled by the heating parameter, $q_w R/k$. This behavior presents itself in Eqn. (5.2) by virtue of the decaying exponential, which leaves only the constant and linear terms after its decay. Physically the behavior follows from the thickening of the boundary layer, which occurs differently for different geometries and boundary conditions.

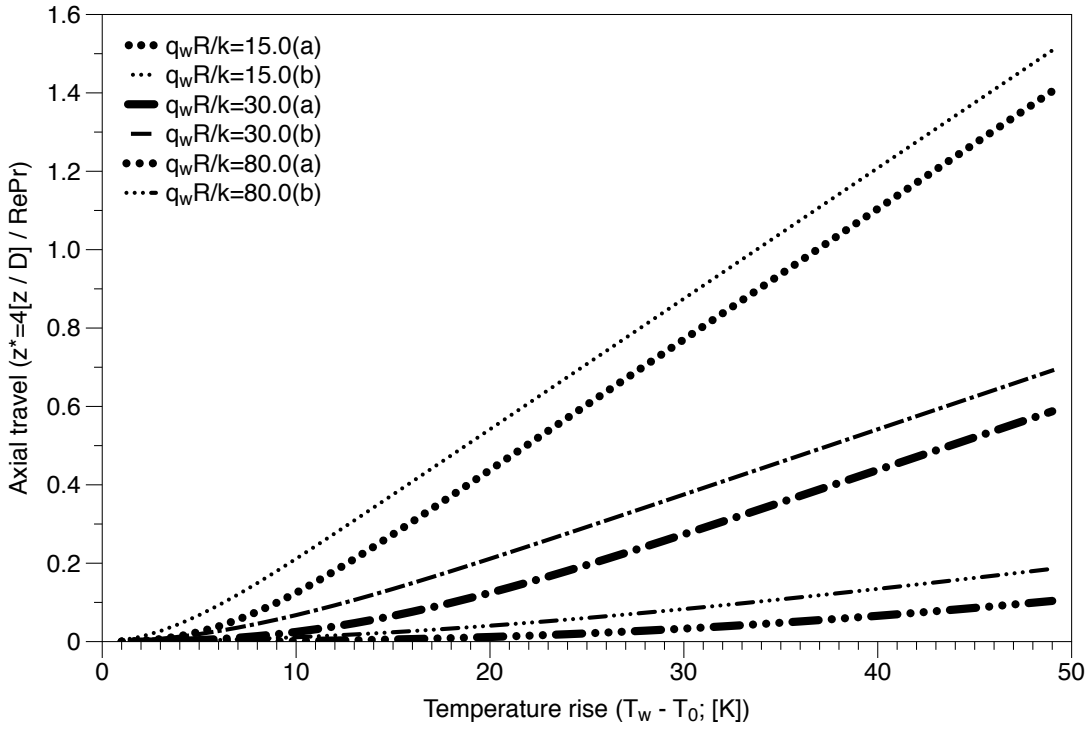

Figure 5.3. Boiling entry length for (a) fully developed and (b) plug flow in a round tube with constant heat flux.

A solution similar to that presented in Figure 5.2 can be generated for numerous cases: constant wall temperature, spatially variable wall temperature, a developing hydrodynamic boundary layer, and many more. The plug flow solution solution in a pipe with constant wall heat flux, accompanied by the fully developed solution (Figure 5.2), may be used to bound the range of boiling entry lengths realized by different hydrodynamic behaviors, and is given by,

$$\frac{T_w - T_0}{q_w R/k} = 2z' + \frac{1}{4} - 2\sum_{n=1}^{\infty} \frac{\exp\left(-\lambda_n^2 z'\right)}{\lambda_n^2}. \tag{5.3}$$

The parametric solution of Eqn. (5.3) appears in Figure 5.3, along with the corresponding solutions from Figure 5.2. The plug flow solution requires a greater

travel distance to achieve the same temperature rise, but in reality the travel distance falls somewhere between the two solutions presented in Figure 5.3. Percent errors in the boiling entry length attributable to improperly prescribing a hydrodynamic condition decrease with increasing temperature rise.

The most accurate solution for a given problem clearly depends on which conditions best emulate reality, but any analytical solution will present errors associated with the transient nature of the boiling front, axial heat conduction in the wall, and other sources of error. Further exploration of these behaviors is required to develop more refined approximations of the boiling entry length. Regardless of future improvement, the fundamental assumption (continuous/dispersed phase temperature equality) used to develop Figures 5.2 and 5.3 is well supported by the simulation results of Chapter 4, and their ease of use make them valuable tools.

5.2 Implications for droplet heat transfer in boundary layers

Performing an Euler-Lagrange simulation of a dilute system requires decisions regarding which aspects of the problem physics to include in the dispersed phase modeling. The results presented in Chapter 4 provide insight into which aspects should be considered when modeling dilute systems in a microchannel.

In one-way coupled Euler-Lagrange calculations, the continuous phase evolution does not depend on the dispersed phase, but the dispersed phase entirely depends on the continuous phase. The results presented in this thesis generally support this type of approach for droplet boundary layer flows, as the droplet influence does not propagate far from the droplet surface. One feature of this coupling deemed entirely necessary based on the present results is inclusion of

the Magnus force, which significantly influences the heating rate of droplets in shear, as shown in Figure 4.13. If the Magnus force is neglected, droplet heating will be accurate for early times, but will over-predict the heating rate and droplet temperature as time progresses.

Though the droplets may be small, the high temperature gradients present in the near-wall region of a microchannel defy the thermally lumped assumption, except for cases when the dispersed phase Prandtl number is small compared to the continuous phase Prandtl number. Typically, the continuous phase has a greater thermal diffusivity than the dispersed phase (as in the case of FC-72 in water). This relation generally applies because the selection of a dispersed phase depends primarily on its boiling point, while the selection of a continuous phase depends primarily on its robustness as a heat transfer fluid. Regardless, a good approximation of the droplet temperature may be obtained by taking the continuous phase temperature at the droplet center, assuming the droplet is absent. In a one way coupled Euler-Lagrange simulation, this assumption is natural because the droplet has already been assumed absent. For increased accuracy, the conduction problem may be solved within the droplet, as in the effective conductivity model. As suggested by the results in Chapter 4, the full Navier-Stokes solution in the droplet differs to a small degree from the conduction problem for small Péclet numbers.

5.3 Conclusions and future work

Simulation of near-wall droplet heating has been performed by means of the Lagrangian volume of fluid interface capturing methodology. An approach for predicting the boiling entry length has been developed, and the simulation results

provide general modeling perspective for near-wall droplet heating.

In the highly viscous near-wall region, internal circulation typically associated with droplet heat transfer is nearly absent. As the Péclet number increases, droplet rolling caused by the velocity difference at the upper and lower surfaces of the droplet becomes more prominent. In the low Reynolds number near-wall regime, this rolling does not significantly influence the droplet heating rate, nor does the droplet presence significantly modify the boundary layer development for Prandtl number ratios near one. For other Prandtl number ratios, the temperature field closely adheres to the conductive field for small Reynolds numbers. Lastly, droplet deformation reduces perturbations to boundary layer development compared to the case of rigid droplets, making low Weber number droplets the most influential in boundary layer development.

Prior to applying the results of this analysis to design, a few areas of future work must be addressed, while others may simply require consideration:

- An experiment must be performed to validate the predicted boiling entry lengths presented in Figures 5.2 and 5.3.

- Although Chapter 4 encompasses the expected Péclet number range for the most rapidly heated droplets in a microchannel, it is desirable to expand the parameter space to greater Péclet numbers. The greater Péclet number range is required to describe the boiling of larger droplets in larger channels.

- Droplet-droplet interactions have been neglected in this analysis by invoking the dilute assumption, but an exploration of these interactions would further inform Euler-Lagrange modeling. It would be important for these interactions to be studied in a three-dimensional, spatially developing environment.

- The dynamics associated with droplet-wall collisions should be described in the context of the boiling entry length.

References

R. Abgrall and S. Karni. Computations of compressible multifluids. *Journal of Computational Physics*, 169:594–623, 2000.

B. Abramzon and W.A. Sirignano. Droplet vaporization model for spray combustion calculations. *International Journal of Heat and Mass Transfer*, 32: 1605–1618, 1988.

T. Ahmad and I. Hassan. Experimental analysis of microchannel entrance length characteristics unsing mircoparticle image velocimetry. *Journal of Fluids Engineering*, 132, April 2010.

M.A. Antar, A.A. Al-Farayedhi, and M.A.I. El-Shaarawi. Steady and transient liquid sphere heating in a convective gas stream. *Heat and Mass Transfer*, 36: 147–158, 2000.

J.C. Berg. *An Introduction to Interfaces and Colloids*. World Scientific Publishing Co. Pte. Ltd., 5 Toh Tuck Link, Singapore 596224, 2010.

J.U. Brackbill, D.B. Kothe, and C. Zemach. A continuum method for modeling surface tension. *Journal of Computational Physics*, 100:335–354, 1992.

L.C. Burmeister. *Convective Heat Transfer*. John Wiley and Sons, Inc, second edition, 1993.

L. Campagnolo, M. Nikolic, J. Perchoux, Y.L. Lim, K. Berling, K. Loubiere, L. Prat, A.D. Rakic, and T. Bosch. Flow profile measurement in microchannel using the optical feedback interferometry sensing technique. *Microfluid Nanofluid*, 14:113–119, 2012.

M. Dai, J.B. Perot, and D.P. Schmidt. Heat transfer within deforming droplets. *Proceedings of ASME: Internal Combustion Engine Division*, 2002.

D.S. Dandy and H.A. Dwyer. A sphere in shear flow at finite reynolds number: effect of shear on particle lift, drag and heat transfer. *Journal of Fluid Mechanics*, 206:381–410, 1990.

B. Frackowiak, G. Lavergne, C. Tropea, and A. Strzelecki. Numerical analysis of the interactions between evaporating droplets in a monodisperse stream. *International Journal of Heat and Mass Transfer*, 23:1392–1401, 2010.

M.A. Hader and M.A. Jog. Effect of droplet deformation on heat transfer to a drop suspended in an electric field. *Transactions of the ASME*, 101:682–689, 1998.

J.F. Harper and D.W. Moore. The motion of a spherical liquid drop at high reynolds number. *Journal of Fluid Mechanics*, 32:367–391, 1968.

C.W. Hirt and B.D. Nichols. Volume of fluid (vof) method for the dynamics of free boundaries. *Journal of Computational Physics*, 39:201–225, 1981.

K.A. Hoffmann and S.T. Chiang. *Computational Fluid Dynamics*, volume 1. Engineering Education System, Wichita, Kansas, 4 edition, 1989.

L.J. Huang and P.S. Ayyaswamy. Heat transfer of a nuclear reactor containment spray drop. *Nuclear Engineering and Design*, 101:137–148, 1987.

L.E. Johns and R.B. Beckmann. Mechanism of dispersed-phase mass ransfer in visous, single-drop extraction systems. *AlchE Journal*, 12:10–16, 1966.

S.G. Kandlikar, S. Colin, Y. Peles, S. Garimella, R.F. Pease, J.J. Brander, and D.B. Tuckerman. Heat transfer in microshannels - 2012 status and research needs. *Journal of Heat Transfer*, 135:18 pages, 2013.

M. Kiya, S. Fukusako, and M. Arie. Effect of non-uniform inlet velocity profile on the development of a laminar flow between parallel plates. *Bulletin of the JSME*, 15(81):324–336, 1972.

R. Kronig and J.C. Brink. On the theory of extraction from falling droplets. *Journal of Applied Science Research*, A2:142–154, 1951.

J. Li, Y.Y. Renardi, and M. Renardy. Numerical simulation of breakup of a viscous drop in simple shear flow through a volume-of-fluid method. *Physics of Fluids*, 12(2):269–282, 2000.

M.B. Liu and G.R. Liu. Smoothed particle hydrodynamics (sph): an overview and recent developments. *Archives of Computational Methods in Engineering*, 17:25–76, 2010.

W. Liu. *Advanced simulation and modeling of turbulent sprays.* PhD thesis, University of Minnesota, March 2014.

W. Liu, E.A. Wenzel, S.C. Garrick, M. Cloeter, and S. Ramalingam. A lagrangian volume of fluid methodology for the simulation of turbulent multiphase flows. *In preparation*, 2014.

E.E. Michaelides. *Particles, Bubbles and Drops.* World Scientific Publishing Co. Pte. Ltd., 5 Toh Tuck Link, Singapore 596224, 2006.

E.E. Michaelides. *Heat and Mass Transfer in Particulate Suspensions*. Springer, New York, 2013.

E.E. Michaelides and Z. Feng. Heat transfer from a rigid sphere in a nonuniform flow and temperature field. *International Journal of Heat and Mass Transfer*, 37:2069–2076, 1994.

D.W. Moore. The boundary layer on a spherical gas bubble. *Journal of Fluid Mechanics*, 16:161–176, 1962.

J.P. Morris. Simulating surface tension with smoothed particle hydrodynamics. *International Journal for Numerical Methods in Fluids*, 33:333–353, 2000.

H. Niazmand, B.D. Shaw, H.A. Dwyer, and I. Aharon. Effects of marangoni convection on transient droplet evaporation. *Combustion Science and Technology*, 103:219–233, 1994.

R. Nourgaliev, N. Dinh, and T. Theofanous. Direct numerical simulation of compressible multiphase flows: Interaction of shock waves with dispersed multimaterial media. *5th International Conference on Multiphase Flow*, 2004.

S. Osher and J. Sethian. Fronts propagating with curvature-dependent speed: Algorithms based on hamilton-jacobi formulations. *Journal of Computational Physics*, 79:12–49, 1988.

S. Prakash and W.A. Sirignano. Liquid fuel droplet heating with internal circulation. *International Journal of Heat and Mass Transfer*, 21:885–895, 1977.

S. Raghuram, V. Raghavan, D.N. Pope, and G. Gogos. Numerical study of marangoni convection during transient evaporation of two-component droplet

under forced convection environment. *Internation Journal of Heat and Mass Transfer*, 55:7949–7957, 2012.

P.W. Randles and L.D. Libersky. Smoothed particle hydrodynamics: some recent improvements and applications. *Computational Methods in Applied Mechanics and Engineering*, 139:375–408, 1996.

M.L. Roesle. *Boiling of Dilute Emulsions*. PhD thesis, University of Minnesota, June 2010.

M.L. Roesle and F.A. Kulacki. Boiling of dilute emulsions - toward a new modeling framework. *Industrial and Engineering Chemical Research*, 49:5188–5196, 2010.

M.L. Roesle and F.A. Kulacki. An experimental study of boiling in dilute emulsions, part a: Heat transfer. *International Journal of Heat and Mass Transfer*, 55:2160–2165, 2012.

R. Savino and S. Fico. Transient marangoni convection in hanging evaporation drops. *Physics of Fluids*, 16:3738–3754, 2004.

S.S. Sazhin, W.A. Abdelgaffar, P.A. Krutitskii, E.M. Sazhina, and M.R. Heikal. New approaches to numerical modelling of droplet transient heating and evaporation. *International Journal of Heat and Mass Transfer*, 48:4215–4228, 2005.

S.S. Sazhin, T. Kristyadi, W.A. Abdelghaffar, and M.R. Heikal. Models for fuel droplet heating and evaporation: Comparative analysis. *Fuel*, 85:1613–1630, 2006.

F.V. Sirotkin and J.J. Yoh. A new particle method for simulating breakup of liquid jets. *Journal of Computational Physics*, 231:1650–1674, 2012.

E.M. Sparrow, S.H. Lin, and T.S. Lundgren. Flow development in the hydrodynamic entrance region of tubes and ducts. *Physics of Fluids*, 7(3):338–347, 1964.

H.A. Stone, B.J. Bentley, and L.G. Leal. An experimental study of transient effects in the breakup of viscous drops. *Journal of Fluid Mechanics*, 173:131–158, 1986.

T.R. Thome. State-of-the-art overview of boiling and two-phase flows in microchannels. *Heat Transfer Engineering*, 27:4–19, 2006.

D.B. Tuckerman and R.F.W. Pease. High-performance heat sinking for vlsi. *IEEE Electron Device Letters*, EDL-2(5):126–129, 1981.

S.C. Wong and A.C. Lin. Internal temperature distributions of droplets vaporizing in high-temperature convective flows. *Journal of Fluid Mechanics*, 237:671–687, 1992.

J.H. Xu, J. Tan, S.W. Li, and G.S. Luo. Enhancement of mass transfer performance of liquid-liquid system by droplet flow in microchannels. *Chemical Engineering Journal*, 141:242–249, 2008.